

ADVANCEMENTS IN VACUUM PROCESS MOLDING AND CASTING

Except where reference is made to the work of others, the work described in this thesis is my own or was done in collaboration with my advisory committee. This thesis does not include proprietary or classified information.

Johnathon Capps

Certificate of Approval:

Sushil H. Bhavnani
Professor
Mechanical Engineering

Ruel A. Overfelt, Chair
Professor
Mechanical Engineering

Lewis N. Payton
Assistant Research Professor
Industrial and Systems Engineering

Stephen L. McFarland
Acting Dean
Graduate School

ADVANCEMENTS IN VACUUM PROCESS MOLDING AND CASTING

Johnathon Capps

A Thesis

Submitted to

The Graduate Faculty of

Auburn University

In Partial Fulfillment of the

Requirements for the

Degree of

Master of Science

Auburn, Alabama

August 8, 2005

ADVANCEMENTS IN VACUUM PROCESS MOLDING AND CASTING

Johnathon Capps

Permission is granted to Auburn University to make copies of this thesis at its discretion, upon request of individuals or institutions and at their expense. The author reserves all publication rights.

Signature of Author

Date

Copy sent to:

Name _____ Date

VITA

Johnathon Capps, son of Randy Capps and Janice Lightsey, was born on September 15, 1979, in Birmingham, Alabama. He graduated McAdory High school with an 'Advanced Academic Diploma'. He then attended Auburn University where he obtained a Bachelors of Science in Mechanical Engineering in August 2002. In August 2002, he then entered Graduate School at Auburn University.

THESIS ABSTRACT

ADVANCEMENTS IN VACUUM PROCESS MOLDING AND CASTING

Johnathon Capps

Master of Science, May 10, 2005
(B.S., Auburn University, 2002)

104 Typed pages

Directed by Ruel A. Overfelt

Vacuum assisted molding, or 'V' Process molding, possesses many benefits over other sand casting processes. However, the process lacks the high cooling rates and speed of solidification that other sand casting processes have. The research in this thesis includes the comparison of the solidification times between three different mold medias, theoretical estimation of the effective thermal conductivity of each mold media, predictions of solidification times and secondary dendrite arm spacings, as well as the casting of a cored valve plate using 'V' Process Molding.

Step patterns, with step volumes of 41 cm³, 82 cm³, 123 cm³, and 164 cm³, were cast using aluminum A356.2 in three different mold medias: silica sand, zircon sand, and copper particulate. The solidification times of each step were theoretically predicted using a number of models available in the literature and compared with experimental

data. Secondary dendrite arm spacings were also estimated from several theoretical models and compared with measured secondary dendrite arms from the experimental castings. Statistical analyses were performed to discern any significant difference between the solidification times of the aluminum alloy in each of the molds.

A cored valve plate was also successfully cast in A356.2 aluminum alloy and AZ91E magnesium alloy using the V-Process. For the casting of magnesium, a standard operating procedure was prepared to safely avoid all potential hazards of the magnesium metal.

ACKNOWLEDGMENTS

I would like to thank Dr. Ruel A. Overfelt for his support and guidance throughout my graduate career. The traits that Dr. Overfelt has taught me will be invaluable throughout my career. I would also like to thank Dr. Lewis Peyton, Dr. Sushil Bhavnani, Dr. Sayavur Bakhityarov, and Dr. Rick Williams for the help, advice and guidance given to me.

Thank you to of my friends who have made my years at Auburn University very memorable and entertaining.

I especially like to thank my mother, father, and the rest of my family for their unyielding support throughout not only my academic career but my entire life. Also, a special thank you to Howard Lightsey for your unconditional encouragement. Your strength and character has and always will be an inspiration to me.

Style manual or journal used: Journal of Material Processing Technology

Computer software used: Microsoft Word 2000, Microsoft Excel 2000, SAS, and Solidedge

TABLE OF CONTENTS

LIST OF TABLES.....	xi
LIST OF FIGURES.....	xiv
1. INTRODUCTION	1
2. LITERATURE REVIEW	4
2.1 Vacuum-Process Mold and Casting.....	4
2.2 Molding Materials.....	7
2.3 Heat Transfer in Molds	8
2.3.1 Methods for Predicting Solidification Time of Metal.....	9
2.3.2 Models for Predicting Effective Thermal Conductivity (ETC) of Packed Beds.....	11
2.4 Grain Structure of Castings.....	14
2.4.1 Secondary Dendrite Arm Spacing and Cooling Rate	16
3. EXPERIMENTAL PROCEDURES	22
3.1 Mold Formation	22
3.1.1 Pattern	22
3.1.2 Mold Formation	23
3.1.3 Sand Core Preparation for Cored Valve Plate	28
3.1.4 Mold Particulate	30
3.2 Metal Casting Practices.....	34
3.3 Temperature Measurements	36
3.3.1 Thermocouple Placement and Data Acquisition.....	36
3.3.2 Cooling Rate Determination	37
3.3.3 Al-Si Phase Diagram.....	38

3.4	Metallographic Sample Preparation.....	41
3.5	Secondary Dendrite Arm Spacing Measurements	41
4.	RESULTS AND DISCUSSION.....	43
4.1	Cooling Rate Comparison of Molds	43
4.2	Thermal Analysis – Theoretical Prediction of Solidification Times	50
4.3	Secondary Dendrite Arm Spacing Measurements	56
4.4	‘V’-Process Development for a Complex Cored Casting.....	63
4.4.1	Casting of a Cored Valve Plate in Aluminum A356.2 Alloy	63
4.4.2	Casting of the Cored Valve Plate in Magnesium AZ91 Alloy	69
5.	SUMMARY AND CONCLUSION	71
5.1	Cooling Rate Comparison of Molds	71
5.2	Theoretical Prediction of Solidification Times	71
5.3	Theoretical Prediction of Secondary Dendrite Arm Spacings	72
5.4	Cored Valve Plate	72
6.	FUTURE RESEARCH.....	74
	REFERENCES	75
	Appendix-A: Detailed Views of Step Casting Pattern.....	78
	Appendix-B: Standard Operating Procedure for Melting and Casting Magnesium	80
	Appendix-C: F ₀ Statistics.....	84
	Appendix-D: Statistical Analysis between SDAS Prediction Models.....	85

LIST OF TABLES

Table 1: Murton and Buhr's Cooling Data [5]	7
Table 2: Emadi and Whiting's values for constants 'a' and 'C' [19]	18
Table 3: Bamberger's Constant, A_{Si} [20]	19
Table 4: Composition of Aluminum A356.2	34
Table 5: Composition of AZ91 Magnesium Alloy.....	35
Table 6: Total number of secondary dendrites measured	42
Table 7: Thermal Conductivity of Casting Molds	43
Table 8: Experimentally Determined Solidification Time in Seconds for 3 Aluminum A356.2 Castings in Silica Sand Molds	45
Table 9: Experimentally Determined Solidification Time in Seconds for 3 Aluminum A356.2 Castings in Zircon Sand Molds.....	46
Table 10: Experimentally Determined Solidification Time in Seconds for 3 Aluminum A356.2 Castings in Copper Particulate Molds.....	47
Table 11: Solidification Time Differences: Silica - Zircon Sand Molds	49
Table 12: Solidification Time Differences: Silica Sand – Copper Particulate Molds	50
Table 13: Solidification Time Differences: Zircon Sand – Copper Particulate Molds.....	50
Table 14: Values used for Effective Thermal Conductivity (ETC) Estimates	50
Table 15: Effective Thermal Conductivity Estimates.....	51
Table 16: Geometric Properties of the Cast Steps	51

Table 17: Thermophysical Properties of the Mold Materials [24]	52
Table 18: Molten Aluminum Thermophysical Properties [24].....	52
Table 19: Predicted Solidification Times	55
Table 20: Statistics Comparing Gori and Corasaniti's ETC Model.....	56
Table 21: Statistics Comparing Chiew and Glandt's ETC Model.....	56
Table 22: Experimentally Determined SDAS for Silica Sand Mold	59
Table 23: Experimentally Determined SDAS for Zircon Sand Mold.....	59
Table 24: Experimentally Determined SDAS for Copper Particulate Mold	59
Table 25: Predicted SDAS Using Bamberger's Empirical Model	61
Table 26: Predicted SDAS Using Kirkwood's Theoretical Model.....	61
Table 27: Predicted SDAS Using Emadi and Whiting's Empirical Model.....	61
Table 28: Predicted SDAS Using Spear and Gardner's Empirical Model.....	61
Table C-29: F_o Values from Statistical Comparisons between Mold Solidification Times	84
Table C-30: F_o Values from Statistical Comparison between Predicted Solidification Time, Obtained from Chiew and Glandt's Model [14] for ETC Estimation, and Experimentally Determined Solidification Time.	84
Table C-31: F_o Values from Statistical Comparison between Predicted Solidification Time, Obtained from Gori and Corasaniti's Model [10] for ETC Estimation, and Experimentally Determined Solidification Time.	84
Table D-32: Statistical Comparison Between Theoretical and Experimentally Determined SDAS For Silica Sand Molds	85

Table D-33: Statistical Comparison Between Theoretical and Experimentally Determined SDAS For Zircon Sand Molds	85
Table D-34: Statistical Comparison Between Theoretical and Experimentally Determined SDAS For Copper Particulate Molds.....	86
Table D-35: F_o Values from comparison between SDAS from theoretical models and experimentally determined in a copper particulate mold.....	87
Table D-36: F_o Values from comparison between SDAS from theoretical models and experimentally determined in a silica sand mold.....	87
Table D-37: F_o Values from comparison between SDAS from theoretical models and experimentally determined in a zircon sand mold	88

LIST OF FIGURES

Figure 1: Steps in 'V' Process Casting [2]	6
Figure 2: Three Zones of Freezing in a Casting [15].....	15
Figure 3: Spear and Gardner's SDAS-Solidification Rate Relationship[18]	17
Figure 4: Emadi and Whiting's Log-Log Relationship between Cooling Rate and SDAS [19].....	18
Figure 5: Peres <i>et al.</i> Data Showing SDAS as a Function of Solidification Time for Varying Silicon Contents in Aluminum[21]	21
Figure 6: A) Cope Pattern, B) Drag Pattern, C) Final Shape of Step Test Casting	23
Figure 7: Experimental Apparatus	24
Figure 8: Drag Pattern on Carrier Flask.....	25
Figure 9: Drag Flask on Formed Plastic Film.....	25
Figure 10: Prepared Drag Mold	26
Figure 11: Cope Pattern on Carrier Flask	26
Figure 12: Prepared Cope Mold.....	27
Figure 13: Completely Prepared Mold (Cope and Drag).....	27
Figure 14: Final Cast Product	28
Figure 15: Sand Core Box A) Drag, B) Insert, C) Cope.....	29
Figure 16: Assembled Sand Core Box.....	29
Figure 17: Laempe Laboratory Sand Core Shooter	30

Figure 18: Silica Sand Size Distribution.....	31
Figure 19: Zircon Sand Size Distribution.....	31
Figure 20: Perforated Box on Drag Pattern	32
Figure 21: Perforated Box with Copper Particulate.....	33
Figure 22: Prepared Drag Copper Particulate Mold	33
Figure 23: Specially Designed Steel Crucible for Magnesium Melting.....	35
Figure 24: Thermocouple placement for step casting.....	36
Figure 25: Temperature and Derived Cooling Rate Plotted as a Function of Time	37
Figure 26: Al-Si Phase Diagram [2]	38
Figure 27: (a) Cooling curve of Aluminum A356.2 and (b) Al-Si phase diagram.....	40
Figure 28: Measurements of SDAS in 3rd step of copper mold casting	42
Figure 29: Temperature Profile of Aluminum A356 Cast Step Pattern in Silica Sand Mold	45
Figure 30: Temperature Profile of Aluminum A356 Cast Step Pattern in Zircon Sand Mold	46
Figure 31: Temperature Profile of Aluminum A356 Cast Step Pattern in Copper Particulate Mold	47
Figure 32: Graphical Representation of the Experimentally Determined Solidification Time as a Function of Step Thickness for the Three Mold Medias	48
Figure 33: Comparison of Experimental and Theoretical Solidification Times for Aluminum A356.2 in a Silica Sand Mold.....	53

Figure 34: Comparison of Experimental and Theoretical Solidification Times for Aluminum A356.2 in a Zircon Sand Mold	53
Figure 35: Comparison of Experimental and Theoretical Solidification Times for Aluminum A356.2 in a Copper Particulate Mold	54
Figure 36: Micrograph of Secondary Dendrite Arms from a Step Thickness of 6.35mm	57
Figure 37: Micrograph of Secondary Dendrite Arms from a Step Thickness of 12.7mm	57
Figure 38: Micrograph of Secondary Dendrite Arms from a Step Thickness of 19.05mm	58
Figure 39: Micrograph of Secondary Dendrite Arms from a Step Thickness of 25.4mm	58
Figure 40: SDAS Data vs. Cooling Rate Comparison.....	62
Figure 41: SDAS Data vs. Solidification Time Comparison.....	62
Figure 42: Cored Valve Plate Pattern for (a) Cope and (b) Drag	64
Figure 43: Chaplet Placement on Valve Plate Sand Core.....	65
Figure 44: A Prepared Drag Mold with Sand Cores for Two Cored Valve Plates	66
Figure 45: Plastic Film Formed Over Cope Pattern of Two Cored Valve Plates	67
Figure 46: Post-Casting Aluminum A356.2 Cored Valve Plate	68
Figure 47: Post-Surfacing Aluminum A356.2 Cored Valve Plate.....	68
Figure 48: Final Magnesium Cast of Brake Valve Plates	70
Figure 49: Temperature Profile of Magnesium AZ91 Cast Step Pattern in Silica Mold..	70

1. INTRODUCTION

In 1971, the Kabushiki Kaisha Akita foundry in Japan was investigating different molding methods that would allow the casting of decorative gates and door coverings with intricate detail [1]. These investigations lead to the creation of the molding method known today as the Vacuum Molding Process or simply 'V' Process Molding. It was found that by using 'V' Process Molding, the desired fine detail of vines, woven rice mats, plants, and the bark of trees were accurately transferred into the castings. The ability of the 'V' Process to obtain great dimensional accuracy and such detail in castings spiked much interest from other foundries. Today, 'V' Process molding is used for the casting of thin-sectioned curtain walls, pressure pipefittings, pulleys, bathtubs, railroad bolsters, machine tools, and engine parts just to name a few. The casting size can range from a few ounces up to 10 metric tons. The largest castings made from this molding process are eight-ton ship anchors and forklift counterweights. Metals that are currently being used in 'V' Process molding are aluminum alloys, copper alloys, cast iron, carbon steel, and manganese and stainless steels. In addition, 'V' Process Molding permits the use of internal sand cores.

‘V’ Process molding can be very beneficial to a foundry and the environment.

The benefits of this process are as follows [2]:

- Versatility
- Environmental and safety improvements
- Material savings
- Tooling simplification
- Plant and facilities advantages
- Casting characteristics
- Management and control advantages

There are many variables in the casting process that can be altered in order to modify specific results in the final part. For instance, the modification of a casting’s solidification rate can alter its mechanical properties. The solidification rate is the rate at which metal completes the phase change from liquid to solid. Different methods may be used in order to alter the solidification rate, one being enhancing the heat extraction properties of the mold. This can be accomplished by the addition of moisture or metallic chills into the mold. Unfortunately castings in a ‘V’ Process mold have a slower rate of solidification than other conventional sand casting methods [1].

In the foundry industry, numerous different metals may be used for casting depending upon its application. Aluminum makes up approximately 12% by weight of the metals produced in the casting industry making it the most popular non-ferrous metal [3]. The reason for the interest in aluminum lies in its relatively low melting point, excellent corrosion resistance, high strength, and low specific gravity [3].

There has also been an increase in interest for the production of castings from magnesium because of its structured properties. The weight per unit volume of magnesium is 36% less than that for aluminum and 78% less than iron [4]. Also magnesium's strength-to-weight ratio is the best of any other structural material [4]. Because of the heightened interest in aluminum and magnesium, alloys aluminum A356 and magnesium AZ91 were used in this study.

2. LITERATURE REVIEW

2.1 Vacuum-Process Mold and Casting

'V' Process casting is distinctly different from other sand casting processes as the 'V' Process requires no binders for holding the sand grains together in the mold. Instead, 'V' Process uses a vacuum to enable atmospheric pressure to hold the dry and binder-free sand. 'V' Process molding begins by placing the desired pattern onto a flat vacuum chamber, also known as the 'carrier', as illustrated in Figure 1(a). A pattern of one side of the casting to be produced is attached to the carrier. Small holes through the pattern provide continuous gas paths from the outside of the pattern to the inside of the vacuum chamber. A thin plastic film is then heated and placed over the pattern assembly and allowed to sag onto the top of the pattern assembly, see Figure 1(b). Next, the vacuum chamber is evacuated and atmospheric pressure forms the plastic film around the pattern as shown in Figure 1(c). The plastic film should exhibit a proper balance of elastic and plastic behavior to allow for easy shaping over the pattern and should produce little gas when decomposing in the presence of the molten metal during casting [2]. A second vacuum flask is then placed onto the carrier and dry, binder-free sand poured onto the top of the plastic film filling the flask. Note Figure 1(e). Vibratory compaction of the sand allows the sand to mold the shape of the underlying pattern. A sheet of unheated plastic film is placed on top of the sand-filled flask and the flask's plenum evacuated, Figure

1(f). The vacuum in the carrier/pattern assembly is released. The pattern can then be removed and atmospheric pressure against the top and bottom plastic films rigidly hold the sand in place. The mold for the other side of the part to be cast is prepared in the same manner and the two molds are locked together to create a plastic film-lined void in the shape of the desired part. See Figure 1(h). Molten metal is then poured into the mold and after it has been allowed to cool and freeze, the vacuum in the plenum in both flasks is released allowing the sand to simply fall away from the final part as shown in Figure 1(i). [2]

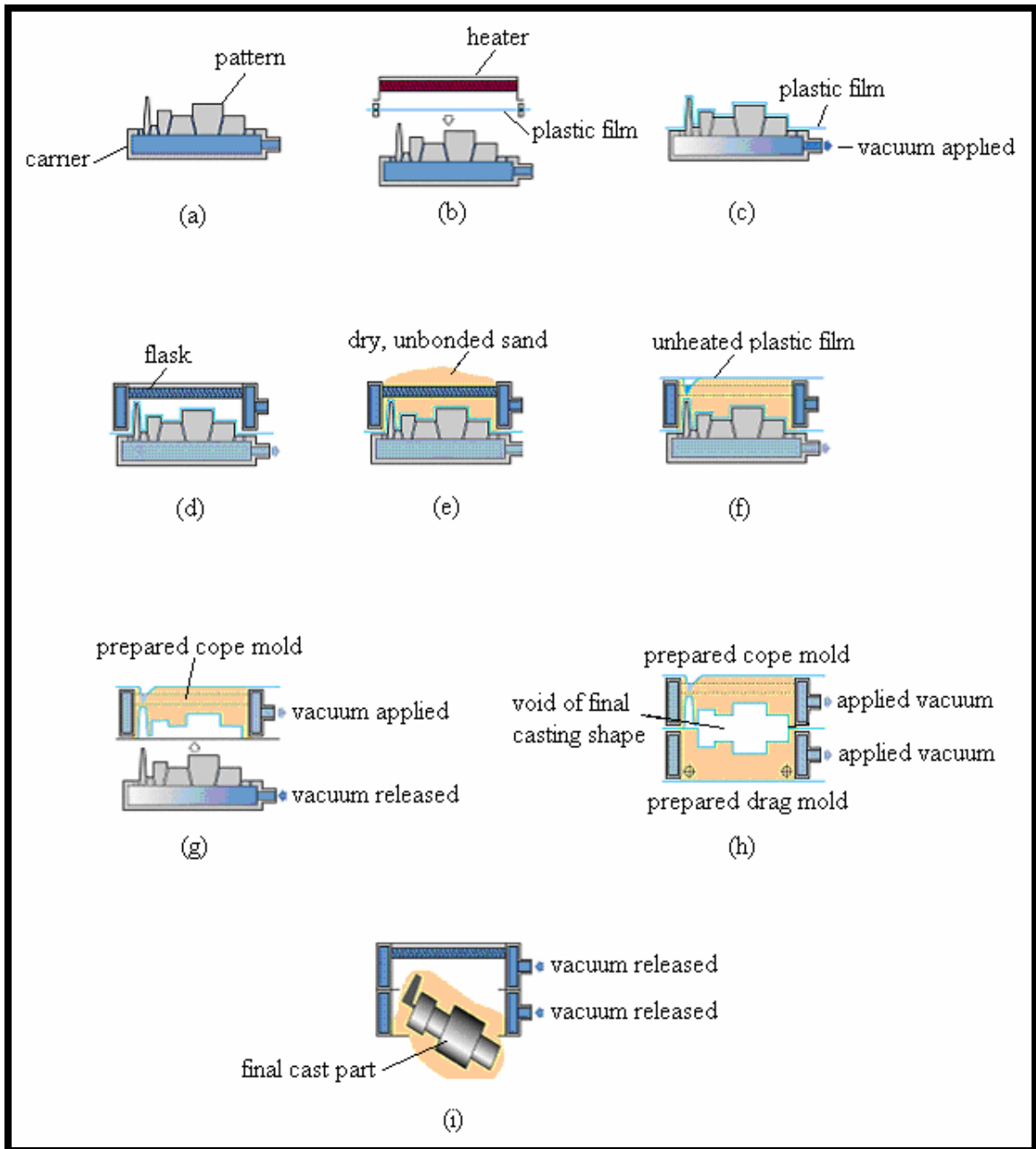


Figure 1: Steps in 'V' Process Casting [2]

2.2 Molding Materials

As noted in the Introduction, ‘V’-process castings typically have lower cooling rates than more conventional casting methods. This aspect was first reported by the Japanese and experimentally quantified by Murton and Buhr [5]. Murton and Buhr produced cast iron bars of 0.5, 1, 1.5, and 2 inches in thickness in traditional green sand (silica sand bonded with clay and moisture) and sodium silicate/CO₂-bonded silica sand molds as well as with ‘V’-process molds using silica and zircon (ZrO₂) sands. Their data are tabulated below:

Table 1: Murton and Buhr's Cooling Data [5]

Cooling Rate Criteria	Section Size, in.	Cooling Rate, °C/second			
		Green Sand	CO ₂ Sand	‘V’ Process	
				Silica	Zircon
1190°-1170°C (Just above eutectic)	0.5	*	*	*	*
	1	4	4	3.33	2.86
	1.5	2	1.82	2.86	1.54
	2	0.91	0.91	0.83	0.95
1170°-1140°C (Through eutectic)	0.5	*	*	*	*
	1	0.27	0.29	0.2	0.18
	1.5	0.13	0.14	0.09	0.08
	2	0.08	0.08	0.05	0.05
1190°-1090°C (Overall)	0.5	2.13	2.56	1.82	1.64
	1	0.72	0.79	0.51	0.46
	1.5	0.36	0.4	0.23	0.23
	2	0.2	0.21	0.13	0.14

Murton and Buhr found that, compared to green sand and sodium silicate-bonded sand molds, there was negligible difference in the cooling rate just above the eutectic of the ‘V’-process castings. However when the overall cooling rate was considered, the ‘V’-process castings appeared to have a lower cooling rate for all section thicknesses. The authors’ rationale for this difference was that since the sand used to form a ‘V’-

process mold is dry, there is no heat removal by the evaporation of moisture as occurs in the more traditional sand molds.

2.3 Heat Transfer in Molds

The transfer of heat from a solidifying molten metal to a porous mold is a very complicated process. The solidification of the molten metal involves conduction through the solid metal as well as convective phenomena within the liquid metal. Within the mold, several heat transfer phenomena can operate including conduction from particle-to-particle in the mold media; gaseous conduction and convection through the air gaps between individual particles of the mold; and radiation from particle to particle through the mold. As noted above, heat from the solidifying metal can also be transported through evaporative cooling of water from moisture in the molds as well as from heats of reaction from the burning of organic binders.

Fleming [6] lists five different regions of thermal resistances to heat transfer from liquid metals being cooled to produce castings:

1. The liquid metal
2. The solidified metal
3. The metal/mold interface
4. The mold
5. The surrounding area around the mold

According to Campbell [7], when compared to low-conductivity sand molds, the resistance to heat flow is negligible due to either (1) the liquid metal or (2) the solid metal or (3) typical gaps between the metal and the mold. Also, most molds are large enough

that they can be considered as semi-infinite solids because there is little difference in temperature between the surface of the mold and its surroundings during the critical times of heat transfer within the casting process. Thus for typical low-conductivity sand molds, the principal resistance to heat transfer in the casting process is the intrinsic thermal conductivity of the mold aggregate.

2.3.1 Methods for Predicting Solidification Time of Metal

The modulus of a casting, M , is defined as:

$$M = \frac{\text{Total Volume of Casting, } V}{\text{Total Surface Area of Casting in Contact With the Mold, } A}. \quad (2.1)$$

In the 1930's, Chvorinov [8] discovered a very interesting and useful relationship between M and the amount of time it takes for molten metal to solidify, t_f . Chvorinov found that there was a linear relationship between t_f and M when plotted on a log-log graph. The specific functional relationship found is:

$$t_f = \frac{p}{4} \left(\frac{\mathbf{r}_s H}{T_s - T_0} \right)^2 \left(\frac{1}{k_m \mathbf{r}_m C_m} \right) (M)^2 \quad (2.2)$$

Where T_s is the temperature of the molten metal, T_0 is the initial temperature of the mold, \mathbf{r}_s is the density of solidifying metal, H is the latent heat of fusion of the metal, k_m is the thermal conductivity of the mold, \mathbf{r}_m is the density of the mold, and C_m is the specific heat of the mold

Though Chvorinov's finding were groundbreaking at the time, he drew criticism for assuming only one-dimensional heat transfer while it is obvious that metal casting is a three-dimensional problem. Also, according to Chvorinov's relation, there would be no

difference in the cooling rate of a molten metal in a spherical mold as opposed to a plate mold. However, according to Trbizan [9] a spherical shape should have a much faster cooling rate than a plate. This prompted an updated relationship that included the effects of differently shaped molds as shown in Flemings [6]:

$$\frac{V}{A} = \frac{2}{\sqrt{\mathbf{p}}} \left(\frac{T_s - T_0}{\mathbf{r}_s H} \right) \left(k_m \mathbf{r}_m C_m \right) \sqrt{t_f} + \left(\frac{n K_m t_f}{2r} \right) \quad (2.3)$$

In this updated expression, the terms n and r describe the casting's geometry and radius, respectively. Values for n are as follows: 0 for a flat plate, 1 for a cylinder, and 2 for a sphere.

From the previous assumption that the mold acts as a semi-infinite solid and due to the small difference in the liquidus temperature and the solidus temperature of aluminum A356.2 (i.e. 8.89°C) leads to the assumption of constant surface temperature of the mold. Thus for a 1-D, semi-infinite mold:

$$q_s''(t) = \frac{k_m (T_s - T_i)}{\sqrt{\mathbf{p} \cdot \left(\frac{k_m}{\mathbf{r}_m \cdot c_{p,m}} \right) \cdot t}} \quad (2.4)$$

where q_s'' is the heat flux through surface per unit area, k_m is the thermal conductivity of the mold, T_s is the surface temperature, T_i is the initial temperature, \mathbf{r}_m is the density of the mold, $c_{p,m}$ specific heat of the mold, t is the time of solidification, and the subscript m denotes the mold.

After integrating Equation 2.4 with respect to time, t , and rearranging the terms:

$$q_s'' = \frac{2k_m(T_s - T_i)\sqrt{t}}{\sqrt{\rho \cdot \left(\frac{k_m}{r_m \cdot c_{p,m}} \right)}} \quad (2.5)$$

Adding the area of heat transfer and setting q_s equal to the product of the amount of mass to solidify, m_f , and the metal's latent heat of fusion, H_f , yields:

$$t = \left(\frac{m_f H_f \sqrt{\rho \cdot \left(\frac{k_m}{r_m \cdot c_{p,m}} \right)}}{2A \cdot k_m (T_s - T_i)} \right)^2 \quad (2.6)$$

Note that if the mass in Equation (2.6) were substituted with the density of the metal multiplied by its volume, Equation (2.6) gives Chvorinov's result.

2.3.2 Models for Predicting Effective Thermal Conductivity (ETC) of Packed Beds

Perhaps the most difficult aspect of predicting the solidification time of a freezing metal is estimating the effective thermal conductivity (ETC) of the mold. A large volume of empirical literature exists on the effective thermal conductivity of a packed bed of beads or particulate. In this current work, three different empirical methods will be utilized for estimating the effective thermal conductivity.

Gori and Corasaniti [10] developed a model to theoretically predict the thermal conductivity of soil at moderately high temperatures. Their model was based on the assumption that one cubic soil particle is at the center of its own unit cell and the rest of the void in the unit cell is filled with a continuous medium of either air or water. Gori

and Corasaniti defined the porosity, ϵ , as the ratio of void volume, V_{void} , to total volume of the cell, V_{cell} . Thus

$$\mathbf{e} = \frac{V_{void}}{V_{cell}} \quad (2.7)$$

By knowing the porosity, Gori and Corasaniti present a variable that is essentially the ratio between the lengths of the unit cell and of the solid particle as:

$$\mathbf{a} = \sqrt[3]{\frac{1}{1-\mathbf{e}}} \quad (2.8)$$

From this variable and knowing the thermal conductivities of the solid phase, k_s , and the void phase (air or water), k_v , the effective thermal conductivity, k_e , can be estimated from the following equation:

$$\frac{1}{k_e} = \frac{\mathbf{a}-1}{k_v \cdot \mathbf{a}} + \frac{\mathbf{a}}{k_v \cdot (\mathbf{a}^2 - 1) + k_s} \quad (2.9)$$

Gori and Corasaniti note that the first term in the above expression considers the thermal resistance of the medium in the cross section and the second term considers the mixture of the solid and the medium.

Peterson and Fletcher present a useful method for estimating the upper and lower limits of the effective thermal conductivity of a porous material [11]. These authors considered a simple weighted average between the solid phase and the liquid (or gas) phase that make up the bulk material. Peterson and Fletcher defined the porosity, ϵ , differently than Gori and Corasaniti.

$$\mathbf{e} = 1 - \left(\frac{\mathbf{r}_b}{\mathbf{r}_s} \right) \quad (2.10)$$

Where r_b is the bulk density of the aggregate liquid and solid phases together and r_s is the density of the solid phase only. To give a lower limit approximation to the ETC of the sintered metal materials, Peterson and Fletcher assumed that the liquid and solid phases transport heat in simple series. With this assumption, the following expression is obtained:

$$k_e^{low} = \frac{k_{void} \cdot k_s}{\mathbf{e} \cdot k_s + k_{void} (1 - \mathbf{e})} \quad (2.11)$$

Conversely, an upper limit approximation to the ETC of the sintered metal materials was obtained by assuming that the liquid and solid phases transport heat in parallel.

$$k_e^{high} = \mathbf{e} \cdot k_{void} + (1 - \mathbf{e})k_s \quad (2.12)$$

In the late 1800's, J.C. Maxwell [12] developed an expression estimating the ETC of randomly distributed spherical particles in a homogeneous medium. The expression given by Maxwell is:

$$k_e = \frac{1 + 2\mathbf{b}\mathbf{e}}{1 - \mathbf{b}\mathbf{e}} k_{void} \quad (2.13)$$

Where ϵ is known as the fractional volume as defined in Equation 2.7. β is termed the reduced thermal polarizability and defined as:

$$\mathbf{b} = \frac{k_s - k_{void}}{k_s + 2k_{void}} \quad (2.14)$$

As explained by Elio Gonzo [13], this model is a very good approximation for the ETC with an ϵ up to 10%. Chiew and Glandt [14] extended Maxwell's equation to much

higher values of ε . Chiew and Glandt's approximation is correct to second order, ε^2 and is:

$$k_e = \frac{1 + 2\mathbf{be} + (K_2 - 3\mathbf{b}^2)\mathbf{e}^2}{1 - \mathbf{be}} k_{void} \quad (2.15)$$

Where K_2 considers the second order contribution. To further the accuracy of this expression, Chiew and Glandt assumed a linear relationship between the two variables K_2 and ε and developed the following expression:

$$k_e = \frac{1 + 2\mathbf{be} + (2\mathbf{b}^3 - 0.1\mathbf{b})\mathbf{e}^2 + 0.05e^{4.5\mathbf{b}}\mathbf{e}^3}{1 - \mathbf{be}} k_{void} \quad (2.16)$$

where e equals 2.718. This expression estimates ETC to an accuracy of the order of ε^3 for values of ε between 0.15 and 0.85 [13].

2.4 Grain Structure of Castings

When molten alloys freeze in molds, three distinctly different microstructural zones can develop: (1) the chill zone in contact with the mold, (2) the columnar zone, and (3) the central equiaxed zone in the middle of the casting. These three zones are illustrated schematically in Figure 2.

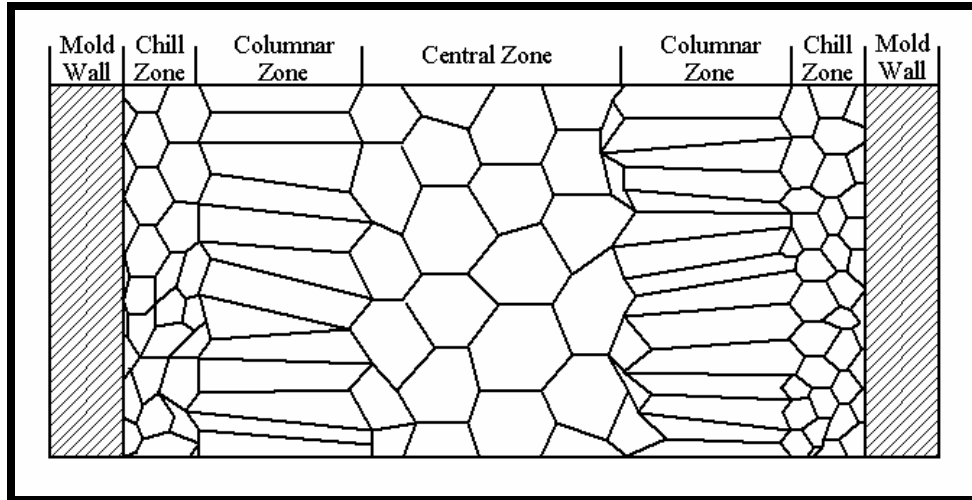


Figure 2: Three Zones of Freezing in a Casting [15].

Large temperature gradients form at the metal/mold interface when molten metal is poured into a mold at much lower temperature. Because of the large temperature gradient, the metal that is in contact with the mold surface cools very rapidly and induces the nucleation of a large number of small equiaxed grains. This thin section of metal that is in contact with the mold surface is called the “Chill Zone”. During the nucleation and growth of the equiaxed grains in the chill zone, the temperature begins to rise due to the release of latent heat. This increase in temperature decreases the local temperature gradient in the solidification region and enables the competitive columnar growth of grains to dominate the nucleation of new grains. This zone is referred to as the “Columnar Zone.” The dendritic growth occurs antiparallel to the heat flow direction and columnar grains grow away from the mold surface. Alloys exhibit a center region called the “Central Equiaxed Zone”. In this zone, the nucleation of equiaxed grains again dominate the freezing process. As the molten alloy solidifies from the mold wall towards

the center, the solute concentrations increase in the liquid, lowering the required temperature for solidification and causing constitutional supercooling.

One major factor that affects the mechanical properties of a casting with an equiaxed grain structure is the secondary dendrite arm spacing (SDAS). It has been shown by Miguelucci [16] and numerous others that as the SDAS decreases, the ultimate tensile strength and elongation increase and *vice versa*. Miguelucci's data show that for an Al-7Si-0.4Mg alloy, a decrease in SDAS from approximately 90 to 30 microns would yield an increase in ultimate tensile strength and elongation of approximately 100 MPa and 7 %, respectively.

2.4.1 Secondary Dendrite Arm Spacing and Cooling Rate

Jefferies and Archer [17] noted in the 1920's that the size of a solidifying cell decreases as the cooling rate of the metal increases. Since this discovery, considerable effort has been expended in order to characterize and predict the size and spacing of secondary dendrites. Motivated by a need for a standardized method for measuring SDAS, Spear and Gardner [18] discovered a log-log linear relationship between SDAS and cooling rate. The relationship was found from plotting the results from several castings of various compositions as duplicated in Figure 3. Thus:

$$\lambda_2 = 0.002 \cdot \left(\frac{dT}{dt} \right)^{-0.337} \quad (2.17)$$

Where λ_2 is the secondary dendrite arm spacing, measured in inches, and dT/dt is the cooling rate, which was measured in °F/second. This empirical relationship was found by casting six different alloys of aluminum: 43, 220, 142, 319, 355, and A356.

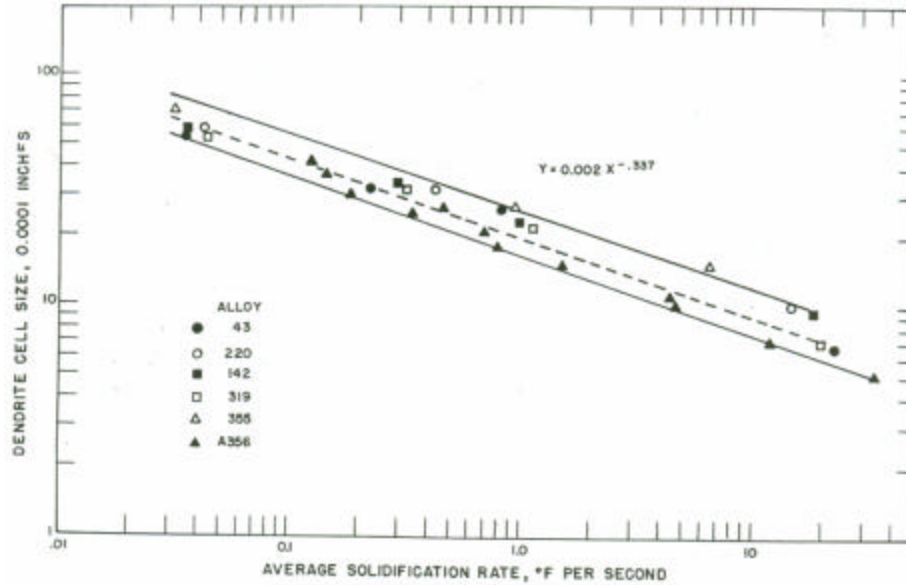


Figure 3: Spear and Gardner's SDAS-Solidification Rate Relationship[18]

Spear and Gardner concluded that the rate at which the aluminum solidified had the largest impact on the growth and spacing of the secondary dendrites.

Emadi and Whiting [19] also conducted several experiments to determine the precise relationship between SDAS and the solidification time in Al-Si alloys. Castings of pure aluminum, Al-3%Si, Al-5%Si, Al-7%Si, Al-9%Si, A356, and A413 were carefully produced and characterized. The SDAS of each casting was measured and plotted versus its corresponding cooling rate, as reproduced in Figure 4. From these results Emadi and Whiting were able to deduce the following relationship:

$$\log(\lambda_2) = a \cdot \log\left(\frac{dT}{dt}\right) + C \quad (2.18)$$

where λ_2 is the secondary dendrite arm spacing, dT/dt is the cooling rate, and 'a' and 'C' are empirically determined constants given in Table 2.

Table 2: Emadi and Whiting's values for constants 'a' and 'C' [19]

Alloy	Slope 'a'	Constant 'C'
pure Al	-0.2096	2.209
Al-3%Si	-0.3621	1.91
Al-5%Si	-0.3153	1.827
Al-7%Si	-0.3383	1.81
Al-9%Si	-0.2537	1.766
A356	-0.3327	1.808
A413	-0.3326	1.789

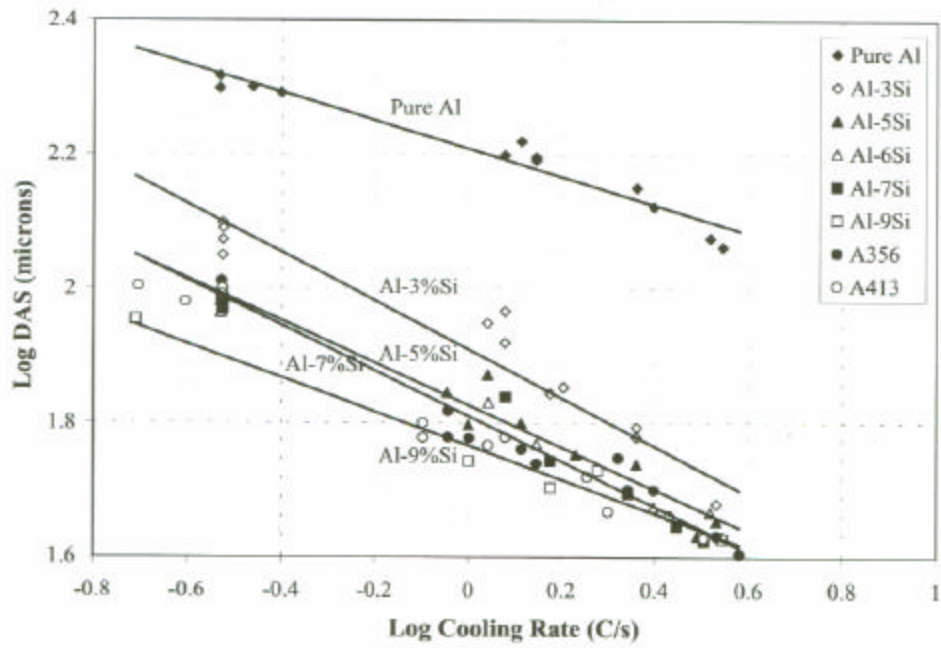


Figure 4: Emadi and Whiting's Log-Log Relationship between Cooling Rate and SDAS [19]

Much like Spear and Gardner, Emadi and Whiting concluded that SDAS decreases with an increase in cooling rate. In addition SDAS decreased as the silicon content increased.

In their work to develop a mathematical model for the heat flow and the SDAS in chill-cast Al-Si alloys, Bamberger *et al.* [20] quantified the relationship between SDAS and local solidification time which differs from Spear and Gardner's and Emadi and Whiting's relationships. Bamberger *et al.* produced aluminum castings of varying silicon content in a silica sand mold. The mold was chilled from underneath with a steel chill. The authors used Al-Si alloys with silicon contents of 3.8, 5.7, 7.5, and 9.7. The measured local solidification time was plotted against its corresponding SDAS. From this plot, Bamberger *et al.* developed the following relationship for the cast Al-Si alloys:

$$\lambda_2 = A_{Si} \cdot t_s^{0.43} \quad (2.19)$$

Where λ_2 is the secondary dendrite arm spacing, t_s is the solidification time, and A_{Si} is a constant. The values of A_{Si} were dependent on the amount of silicon in the aluminum.

The values for A_{Si} are given in Table 3:

Table 3: Bamberger's Constant, A_{Si} [20]

Si, wt-%	3.8	5.7	7.5	9.7
A_{Si}	15.3	14	12.8	11.5

Like the previous researchers before, Bamberger *et al.* concluded that SDAS is highly dependent on the solidification time (i.e. cooling rate) and that an increase in silicon content would cause a decrease in SDAS.

Peres *et al.* [21] also investigated the secondary dendrite arm spacing of several aluminum alloys with silicon contents of 3, 5, 7, and 9%. Peres *et al.* compared the experimental results with theoretical results from models given by Bamberger *et al.* [20] and Kirkwood [22].

Unlike Bamberger's model [20], Kirkwood's model used fundamental material properties rather than a single empirically determined constant. The Kirkwood model is as follows:

$$\lambda_2^3 = M \cdot t_s \quad (2.20)$$

with:

$$M \cong \frac{128DsT}{Hmc_1(1-k)} \quad (2.21)$$

where λ_2 is the secondary dendrite arm spacing, t_s is the solidification time, D is the liquid solute diffusivity, σ is the surface energy, T is the absolute melting point, H is the volumetric heat of fusion, m is the liquidus slope, c_l is the mean composition in liquid region, and k is the solute partition coefficient.

After comparing the theoretical SDAS values with the experimental values, Peres *et al.* found that Kirkwood's model gave a better estimation than Bamberger's model for all four alloys. The SDAS predicted by Bamberger's model overestimated the experimental SDAS for every case as can be seen in Figure 5. Also Peres *et al.* concluded that SDAS were decreased with an increase in solute content.

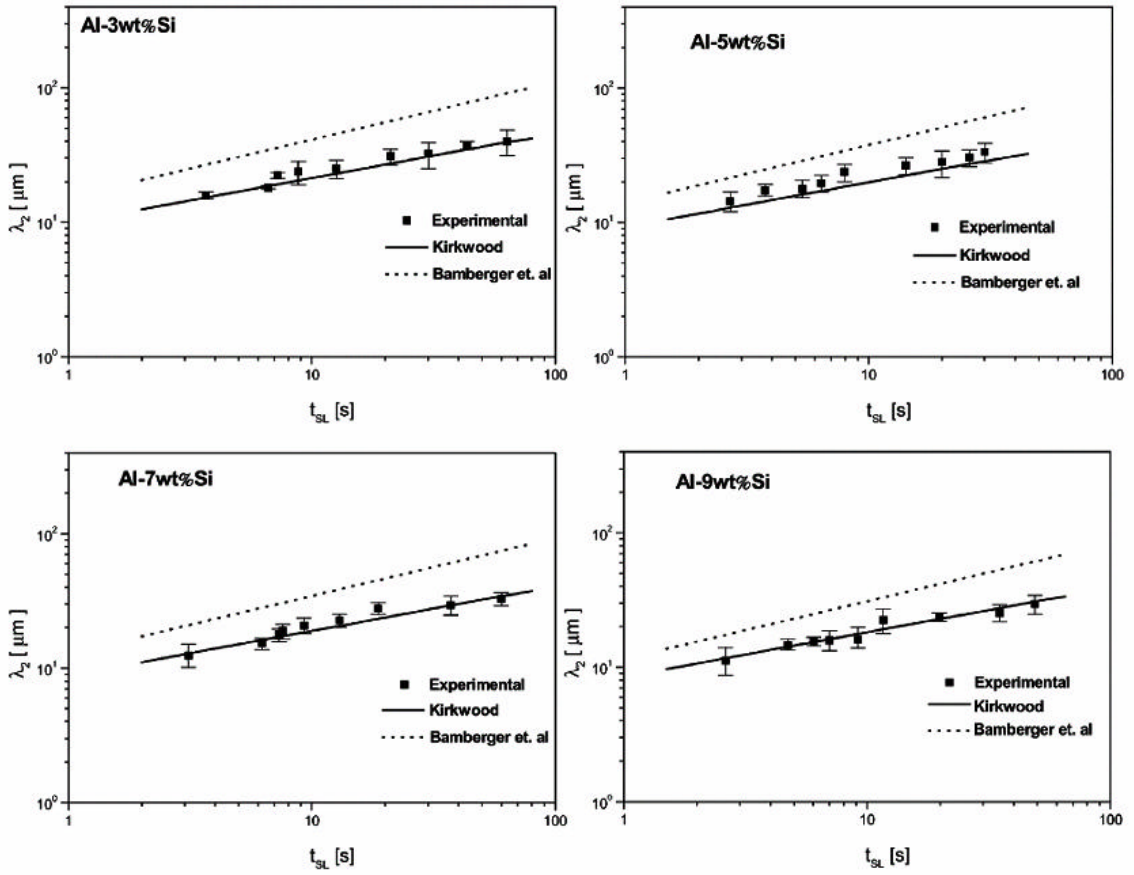


Figure 5: Peres *et al.* Data Showing SDAS as a Function of Solidification Time for Varying Silicon Contents in Aluminum[21]

3. EXPERIMENTAL PROCEDURES

3.1 Mold Formation

3.1.1 Pattern

In order to obtain various cooling rates from each casting, a step pattern of various thicknesses was used for the present experiments. The step pattern consisted of four steps of 50.8 mm in length with thicknesses of 6.35 mm, 12.7 mm, 19.1 mm, and 25.4 mm. The overall width of the step pattern was 127 mm. The parting line for the step pattern was chosen to be between the 6.35 mm step and the 12.7 mm step. Thus the upper (cope) pattern exhibited three steps with thicknesses of 6.35 mm, 12.7 mm, and 19.1 mm and the lower (i.e., drag) pattern consisted of one step 6.35 mm thick (203.2 mm long and 127 mm wide). Detailed views of these patterns are given in the Appendix A. Figure 6 shows (a) upper (cope) pattern, (b) lower (drag) pattern, and (c) final shape of the step test casting.

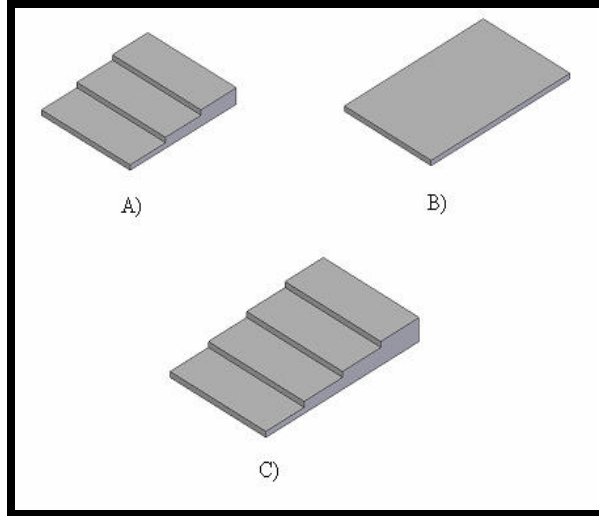


Figure 6: A) Cope Pattern, B) Drag Pattern, C) Final Shape of Step Test Casting

3.1.2 Mold Formation

The upper and lower molds were clamped together forming the ‘V’-Process mold. The equipment used to create the ‘V’ Process mold is shown in Figure 7. Initially, the lower (drag) pattern is placed onto the top of the hollow carrier plate that is 59.7 cm² in total area, Figure 8. A heater is then placed over the top of the carrier and pre-heated to 37.8°C. Once at this temperature, a 3 mm thick sheet of 18% EVA plastic, 70 cm² in area, was placed near the heater for approximately seven seconds to soften it for forming against the lower pattern. After softening, the plastic film was lowered over the pattern and atmospheric pressure molded the plastic film around the pattern. A doubled-wall flask, 59.7 cm² in area with a 5.08 cm thickness, was then placed on top of the plastic film covering the pattern and carrier, Figure 9. The flask was then filled with the media used for that particular experiment: silica sand, zircon sand, or copper particulate. The media was then gravity compacted for 25 seconds using horizontal vibration. Additional plastic film was subsequently placed over the top of the flask and the flask then

evacuated. The carrier vacuum chamber was then opened to the atmosphere and the bottom mold removed from the pattern, Figure 10. The upper mold (cope) was prepared in a similar fashion, Figures 11 and 12. The total pattern consists of the four steps, ingate, runners, sprue, sprue cup, and riser as illustrated schematically in Figure 14.

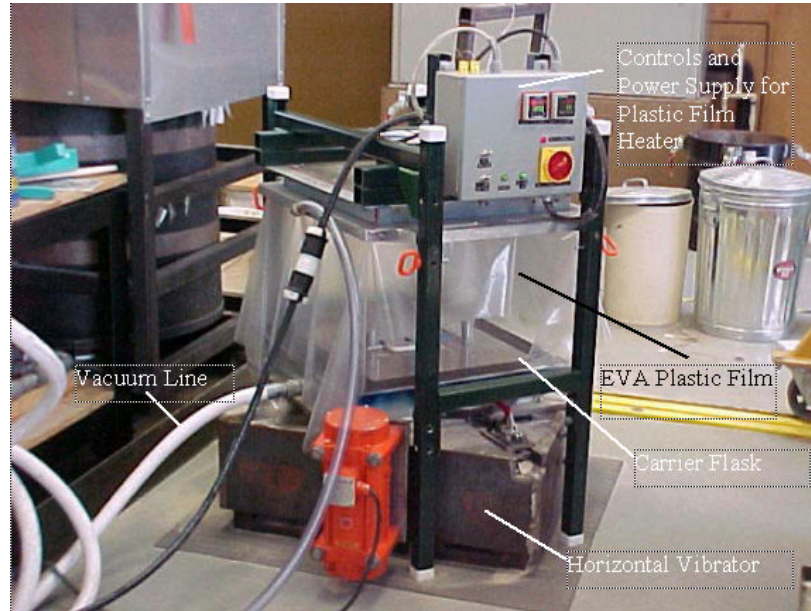


Figure 7: Experimental Apparatus

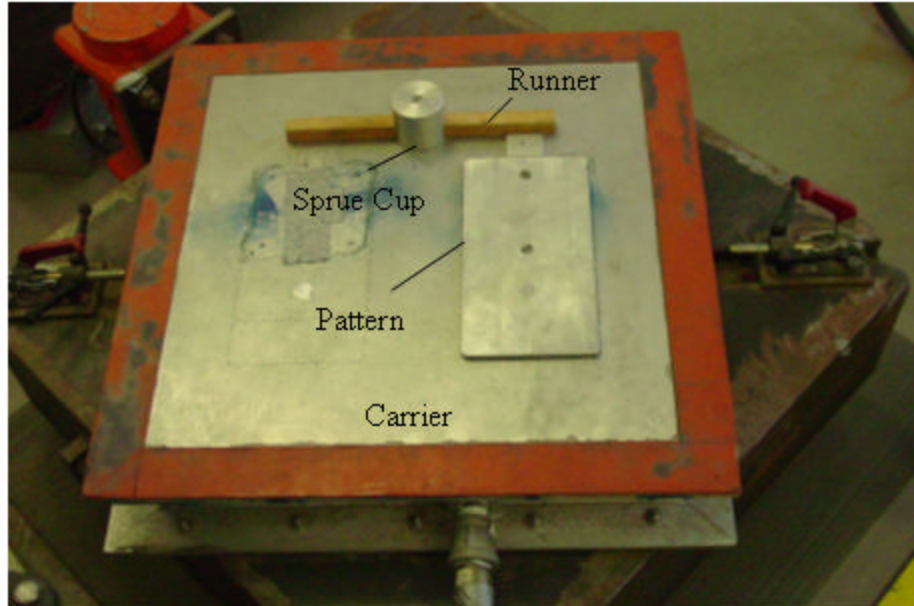


Figure 8: Drag Pattern on Carrier Flask

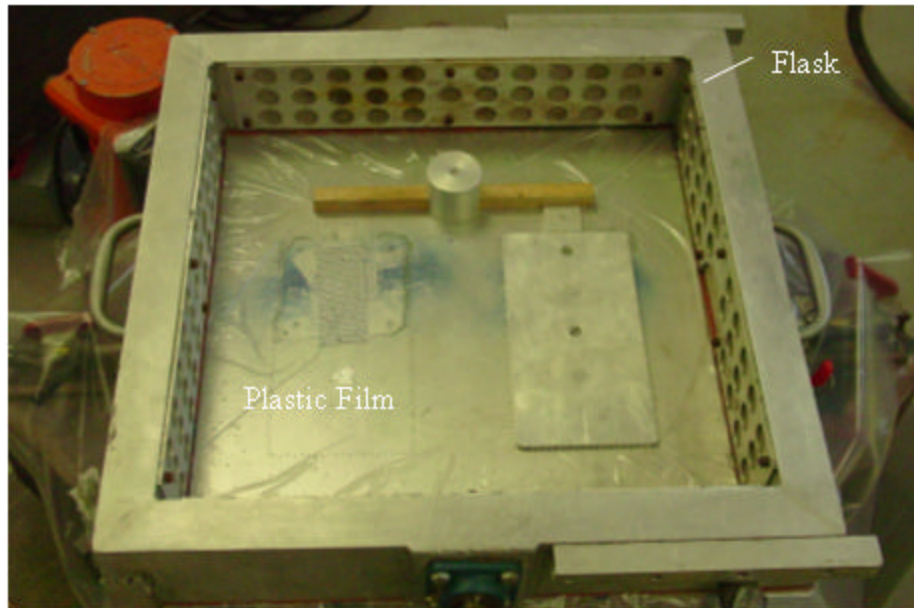


Figure 9: Drag Flask on Formed Plastic Film



Figure 10: Prepared Drag Mold

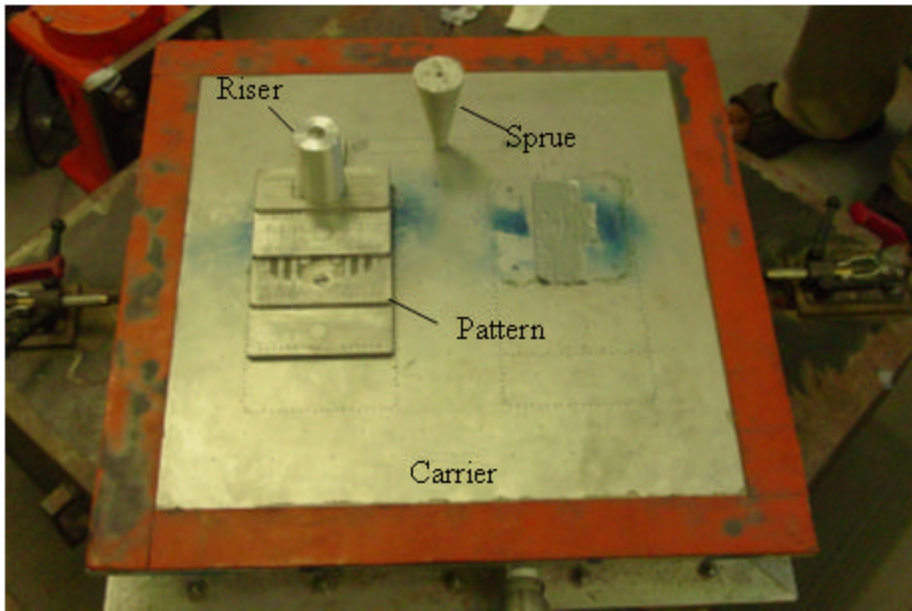


Figure 11: Cope Pattern on Carrier Flask



Figure 12: Prepared Cope Mold

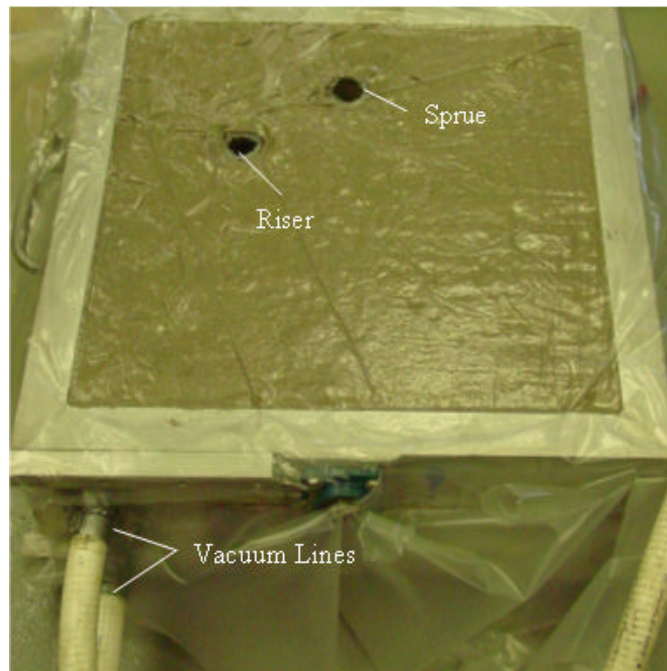


Figure 13: Completely Prepared Mold (Cope and Drag)

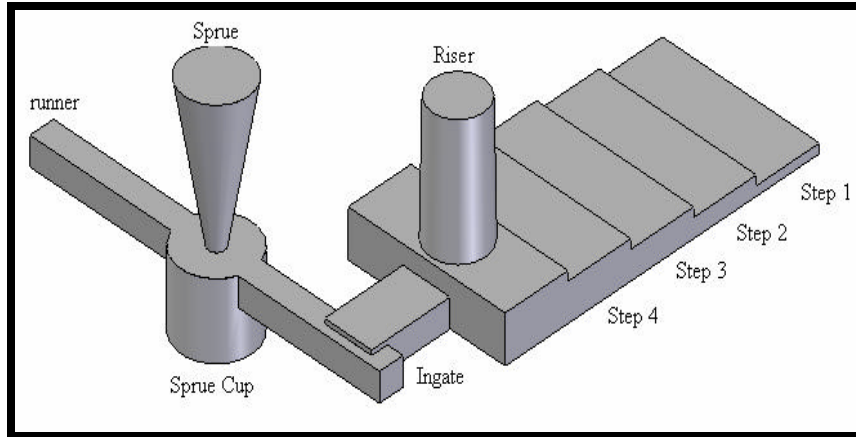


Figure 14: Final Cast Product

3.1.3 Sand Core Preparation for Cored Valve Plate

The sand cores used for the industrial valve plate were made in a specially designed core box. The core box consisted of two halves, a cope and drag as shown in Figure 15. The two halves included vent holes to allow for the evacuation of air when sand was blown into the mold. A metal insert was added between the cope and drag to produce the shape of the sand core. This insert is shown in Figure 15. Once the sand was blown into the mold and the binder cured, the cope and drag were separated, the insert was removed, and the core then safely removed. The sand mixture was prepared with the designated sand and a two-part binder. The three components were thoroughly mixed and placed inside the core shooter. The sand cores were blown using a Laempe laboratory sand core shooter using the phenolic-urethane-amine cold box process. The prepared sand mixture was blown into the three designated holes of the core box and gassed. The gassing caused the binders in the sand to cure.

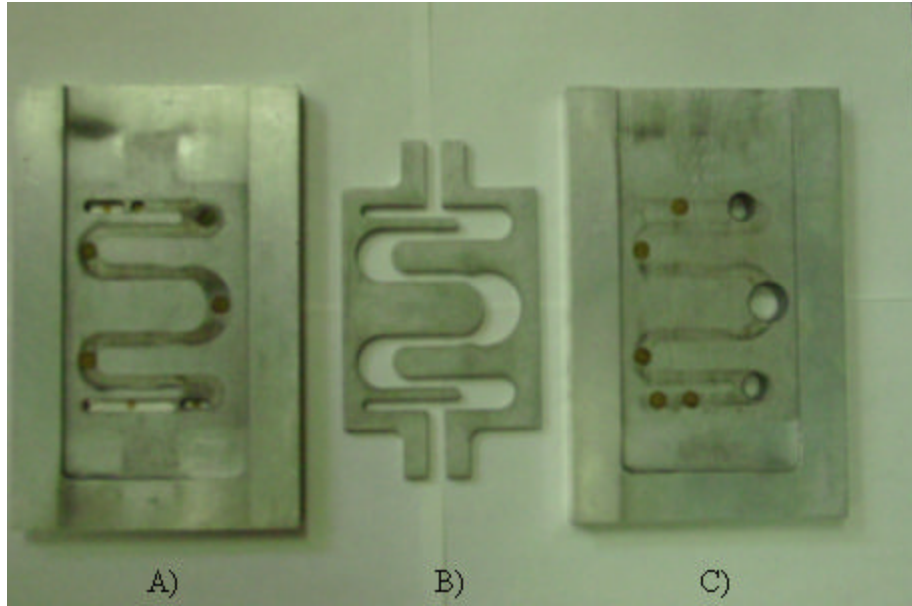


Figure 15: Sand Core Box A) Drag, B) Insert, C) Cope



Figure 16: Assembled Sand Core Box



Figure 17: Laempe Laboratory Sand Core Shooter

3.1.4 Mold Particulate

The affects of different mold media on the cooling rate of the aluminum was evaluated by using molding media of the following particulates: silica sand, zircon sand, and copper particulate. The particle size distribution for the silica and zircon sand was determined experimentally from a vibratory sieving apparatus. One kilogram of sand was placed into the sieve where it was subjected to oscillating vibrations for twenty minutes. This allowed for the separation of sand grains with varying diameters. The sand in each sieve was then weighed and divided by the total amount of sand to

determine the weight percent. The size distribution of the silica and zircon sand used for the experimentation is shown in the Figures 18 and 19, respectively. The copper particulate grains used for experimentation were spherical with a uniform diameter of 0.81mm.

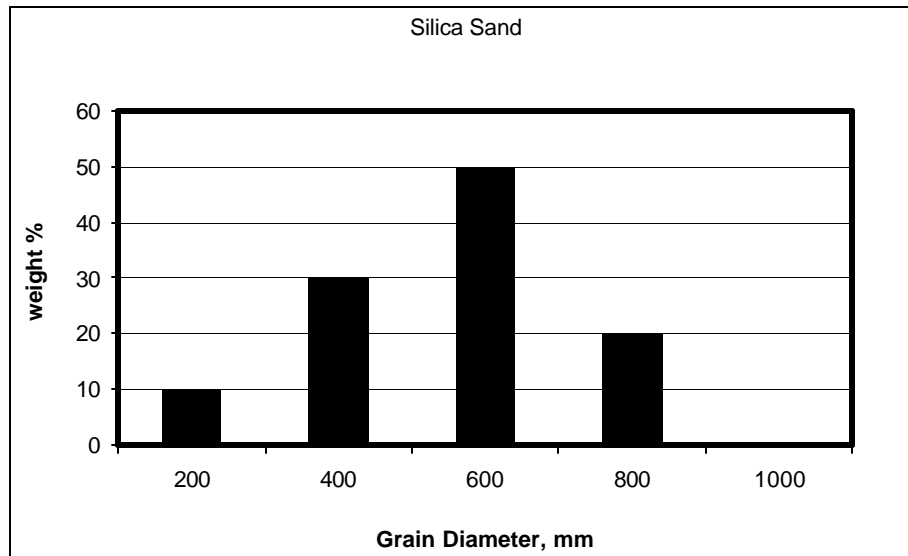


Figure 18: Silica Sand Size Distribution

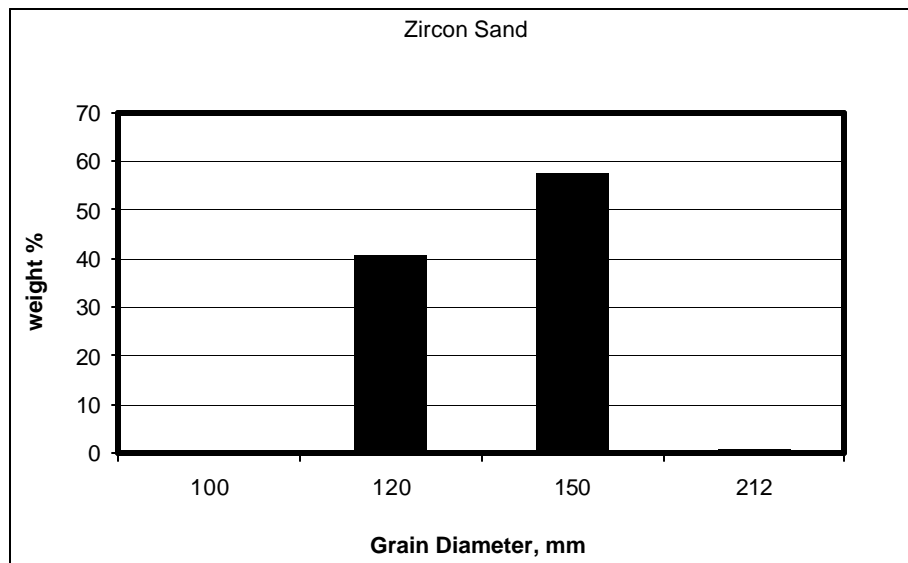


Figure 19: Zircon Sand Size Distribution

Although the pumping capacity of the vacuum pump system was high enough to maintain the shape of a mold with silica or zircon sands, the copper particulate was too dense and the molds deformed when they were lifted. A “composite” mold process was then designed for the copper particulate wherein a fine mesh screen and perforated sheet metal box assembly of dimensions 30 x 23 x 10 cm was placed around the pattern, note Figure 20. Copper particulate was poured on top of the pattern and filled the region contained by the wire screen (Figure 21). This allowed the step pattern to be completely surrounded by the copper particulate. Also, to keep the copper particulate from sticking to the aluminum casting, a thin coat of slurry was applied to the plastic film prior to filling with the copper shot. Silica sand was then used to complete the filling of the ‘V’ Process flask as shown in Figure 22.

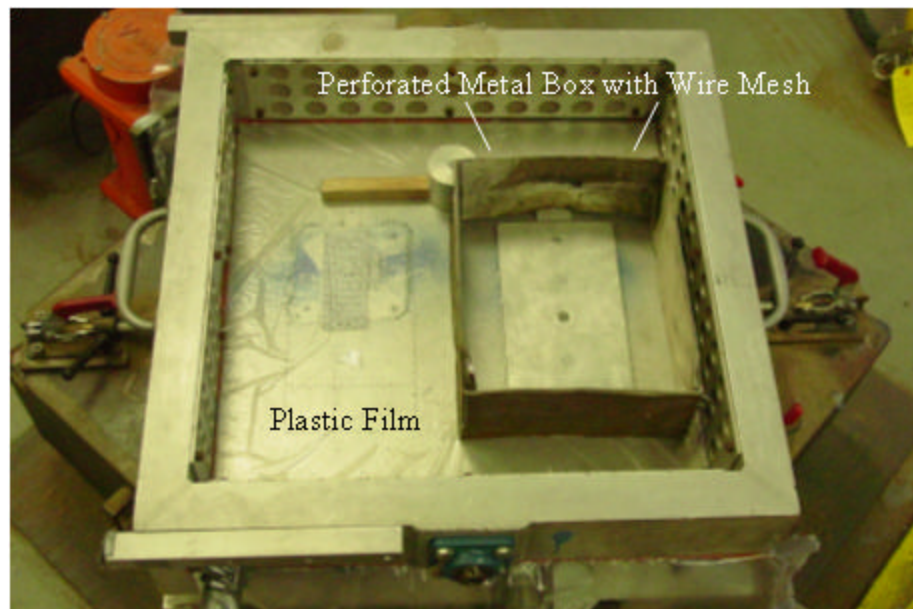


Figure 20: Perforated Box on Drag Pattern

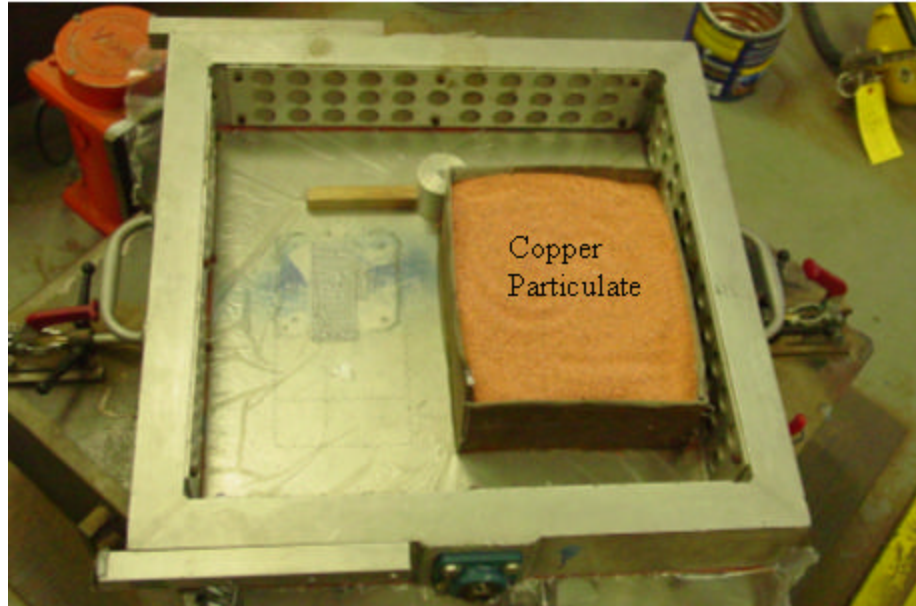


Figure 21: Perforated Box with Copper Particulate



Figure 22: Prepared Drag Copper Particulate Mold

3.2 Metal Casting Practices

The A356.2 aluminum alloy was melted in a silicon-graphite crucible by a 50kW LEPEL[®] induction furnace. The composition of aluminum A356.2 is listed in Table 4 below. Approximately 15 lbs of aluminum alloy were heated to 800°C at which time argon was introduced into the melt via a porous graphite tube for 15 minutes to degas the melt for hydrogen removal. When the melt had cooled to 760°C, 0.015 wt % of strontium was added, the oxide layer on the molten surface was then removed with a steel skimming tool and the aluminum poured into the ‘V’ Process mold cavity.

Table 4: Composition of Aluminum A356.2

	Weight %						
	Al	Si	Mg	Ti	Fe	Cu	Zn
Al A356.2	91.3 - 93.2	6.5 - 7.5	0.3 - 0.45	Max 0.2	Max 0.12	Max 0.1	Max 0.05

The AZ91 magnesium alloy was melted in the same fashion as the aluminum, however, a specially designed protective atmosphere steel crucible was used. The composition of AZ91 magnesium alloy is listed in Table 5 below. The steel crucible can be seen in Figure 23. The crucible was designed to allow an influx of cover gas over the melt to act as a barrier between the molten magnesium surface and the atmosphere. The cover gas used for protecting molten magnesium was a mixture of 99%CO₂+1%SF₆. This cover gas was blown over the molten magnesium, at a rate of 0.3 l/min, where it settled over the top of the melt, separating the melt from the atmosphere. The magnesium was heated to 800°C at which point potassium-fluoroborate was added to the melt for degassing. The oxide layer was removed and the molten magnesium poured into the mold at 760°C.

In addition, the silica sand used for magnesium casting (both molds and cores) contained a special fire inhibitor of 1% by volume of 50% potassium fluoroborate and 50% sulphur.

Table 5: Composition of AZ91 Magnesium Alloy

	Weight %						
	Mg	Al	Zn	Si	Ni	Mn	Cu
Mg AZ91	90	8.1 - 9.3	0.4 - 1.0	Max 0.3	0.01	0.13	Max 0.1

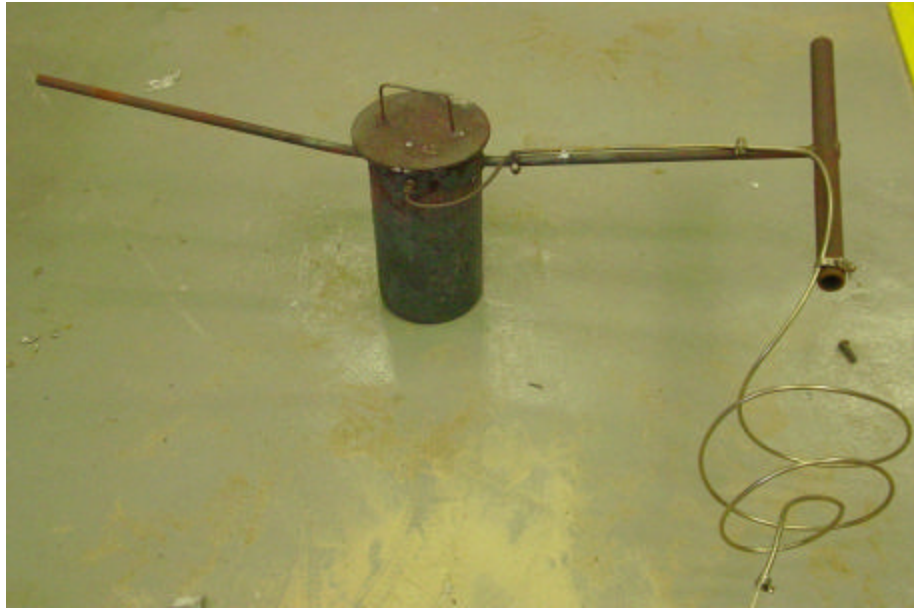


Figure 23: Specially Designed Steel Crucible for Magnesium Melting

3.3 Temperature Measurements

3.3.1 Thermocouple Placement and Data Acquisition

All temperature measurements in the molds were made using K-type, chromel/alumel, thermocouples that were protected by 3.175 mm diameter ceramic sheaths. The diameter of the chromel and alumel wires was 0.508 mm. The thermocouples were placed in the mold cavity lying horizontally on the parting surface and extending into the mold cavity as shown in Figure 24. The thermocouples were connected to a computer controlled data acquisition system via PC-LPM-16/DAQCard-700. The data acquisition scan rate used for the thermocouples was 0.1 Hz.

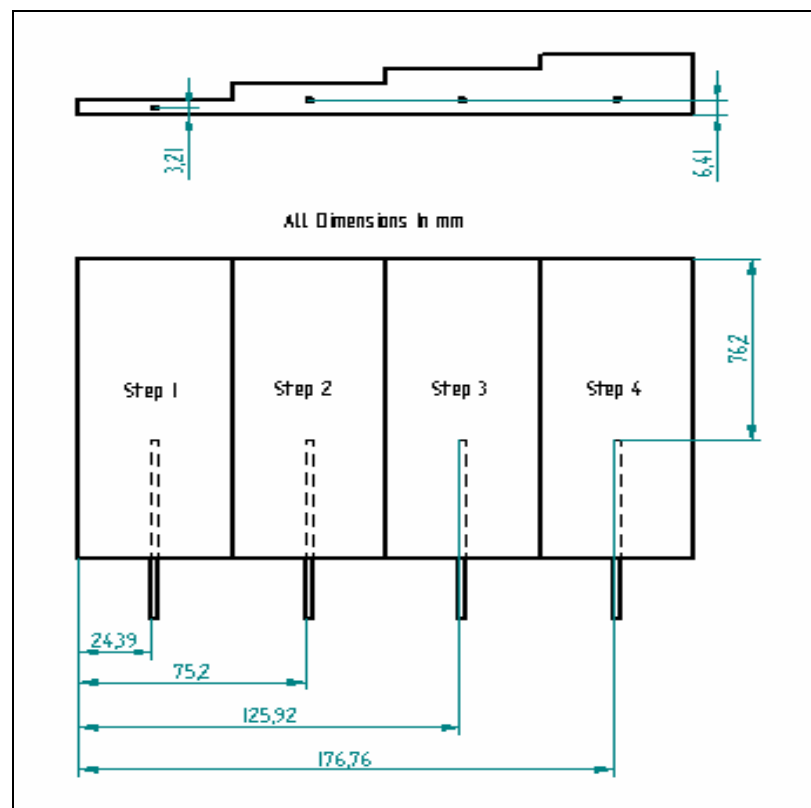


Figure 24: Thermocouple placement for step casting

3.3.2 Cooling Rate Determination

The cooling rate for each step was determined from the raw thermocouple data. Numerical derivatives were estimated as the change in temperature (ΔT) over a one second time period (Δt). The derivatives were then plotted along with the temperature as a function of time as shown by the typical plot illustrated in Figure 25.

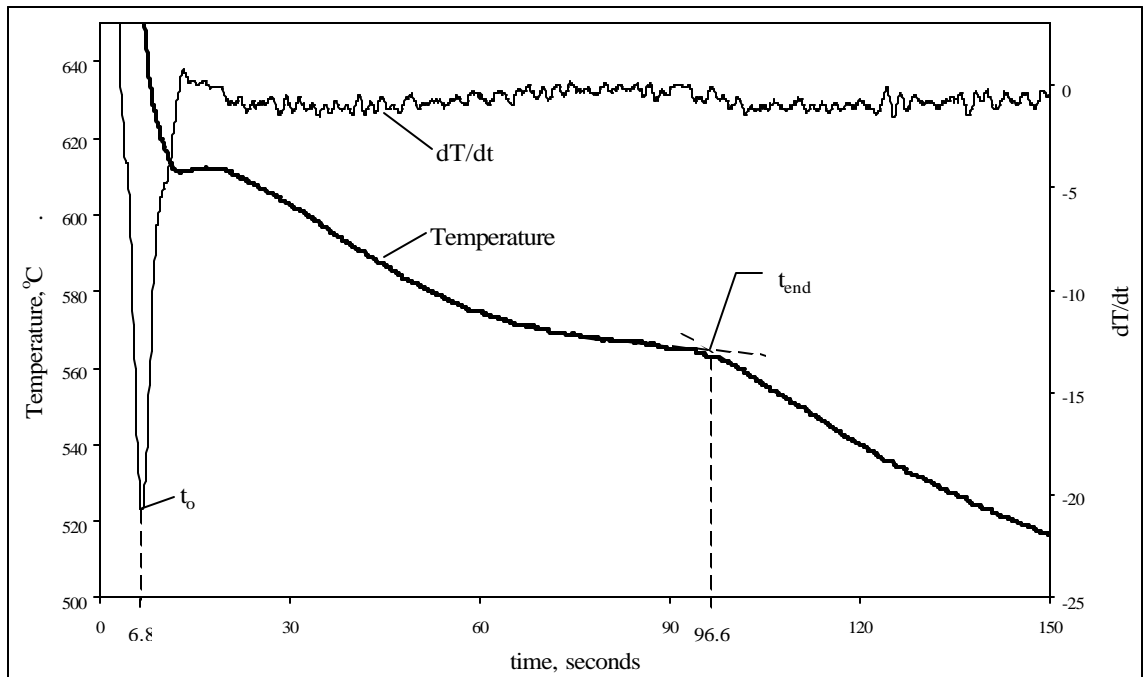


Figure 25: Temperature and Derived Cooling Rate Plotted as a Function of Time

Solidification can be seen to begin at about 6.8 seconds (t_o), which is indicated by the drastic change in cooling rate. The end of the solidification process can be estimated by the intercept of the two tangential lines seen in Figure 25. t_{end} occurs at about 96.6 seconds. Therefore the solidification time t_f is approximately 89.8 seconds. Also the overall cooling rate is the difference in the liquidus and solidus temperatures, 48°C,

divided by the solidification time. Therefore, the average cooling rate of the above step is about 0.535C/second. All cooling rates were estimated using this methodology.

3.3.3 Al-Si Phase Diagram

Phase diagrams are an important tool in understanding the regions of phase changes that occur in alloy systems. Figure 26 shows the binary phase diagram for aluminum and up to 20% silicon. All points above the line labeled liquidus represent a phase of pure liquid. All points in the 'a' region consist of solid solution silicon in aluminum. The points that lie between the liquidus, solidus, and the eutectic temperature, 577 °C, in the 'a+L' region represent a mixture a and liquid. Below the eutectic temperature, the binary alloy has completely solidified.

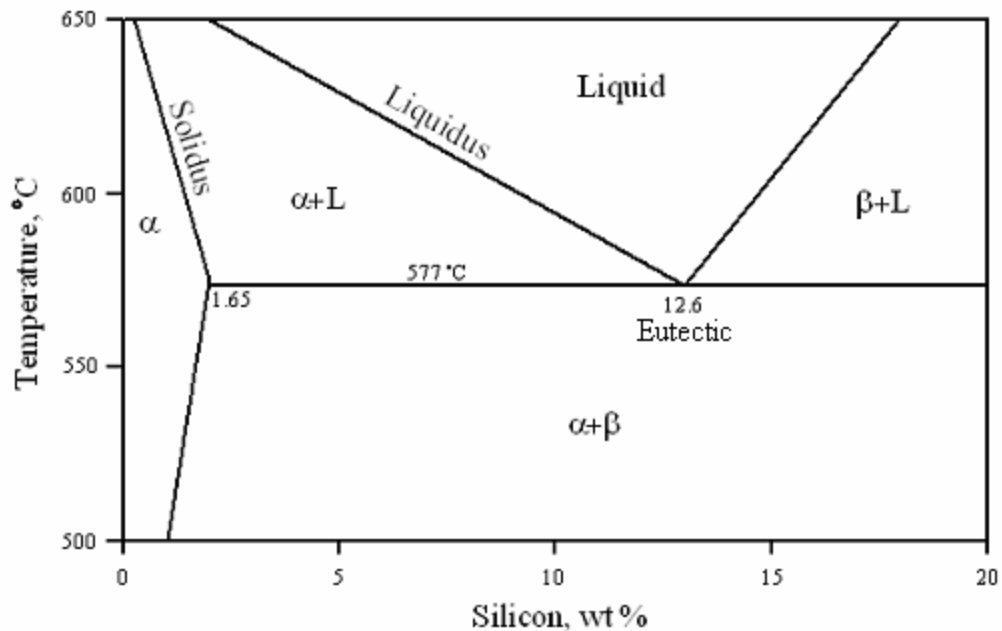


Figure 26: Al-Si Phase Diagram [2]

To show the relationship between the solidification of aluminum A356.2 and its corresponding phase diagram, a cooling plot of the aluminum alloy is shown side by side with the Al-Si phase diagram in Figures 27(a) and 27(b) respectively. Figure 27(b) contains a vertical line drawn at 7% silicon. The intersection of this line with the liquidus line, point A, and the eutectic line, point B, corresponds to the liquidus and solidus temperature, respectively, of aluminum with 7% silicon at equilibrium. The temperatures at the intersections of the liquidus and eutectic lines in Figure 27(b) correspond with the temperatures at the beginning and ending of solidification found in Figure 27(a). The reasons for minor discrepancies between the liquidus and solidus temperatures of two graphs can be attributed to the phase diagram only considering aluminum and silicon and the affects of the other alloying elements in A356 aluminum alloys.

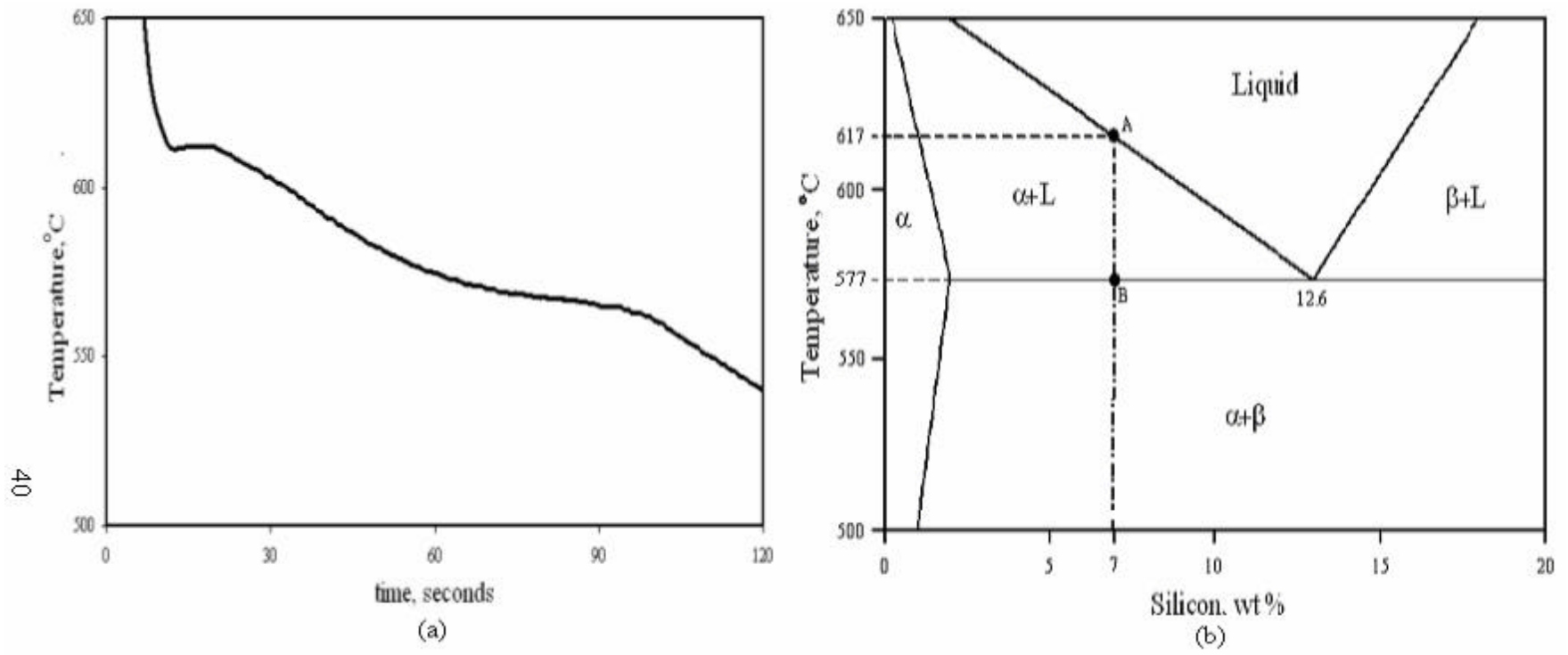


Figure 27: (a) Cooling curve of Aluminum A356.2 and (b) Al-Si phase diagram

3.4 Metallographic Sample Preparation

All metallographic samples were mounted using Durofast resin. Once the resin hardened, the samples were subjected to a grinding process that included the following grit sizes: 240, 400, 600, and 1000 grit paper. After the 1000 grit grinding, the sample was rough polished using a 5-micron diamond spray. Lastly, the sample was finely polished using a 0.05-micron aluminum oxide abrasive. Digital images of the as-polished microstructures of the samples were then taken using an Olympus (PME 3) optical microscope.

3.5 Secondary Dendrite Arm Spacing Measurements

Multiple micrographs were taken from each step in the vicinity of the temperature measurement. The measurement of each sample's secondary dendrite arm spacings was made on a number of micrographs and using a number of well-aligned dendrite arms. An example for one of these micrographs is shown in Figure 28. Measurements were taken along a trail of secondary dendrites, from the midpoint of the first to the midpoint of the last. In the example shown in Figure 28, four secondary dendrite arm trails were measured. The total number of secondary dendrites along the entire length of primary dendrite arms was then determined. For instance, from Figure 28, trail A contains 5 secondary dendrite arms, B contains 4, C contains 3, and D contains 2. The total length of trail A was measured as 3.6-cm, B is 1.9-cm, C is 1.6-cm, and D is 1-cm. At the magnification of Figure 28, the total length of the primary dendrite arms is 540 microns and thus the mean SDAS is 38.6 microns.

All SDAS were measured in this manner. The numbers of secondary dendrites measured in this study, for each casting and each step, are shown in the Table 6.

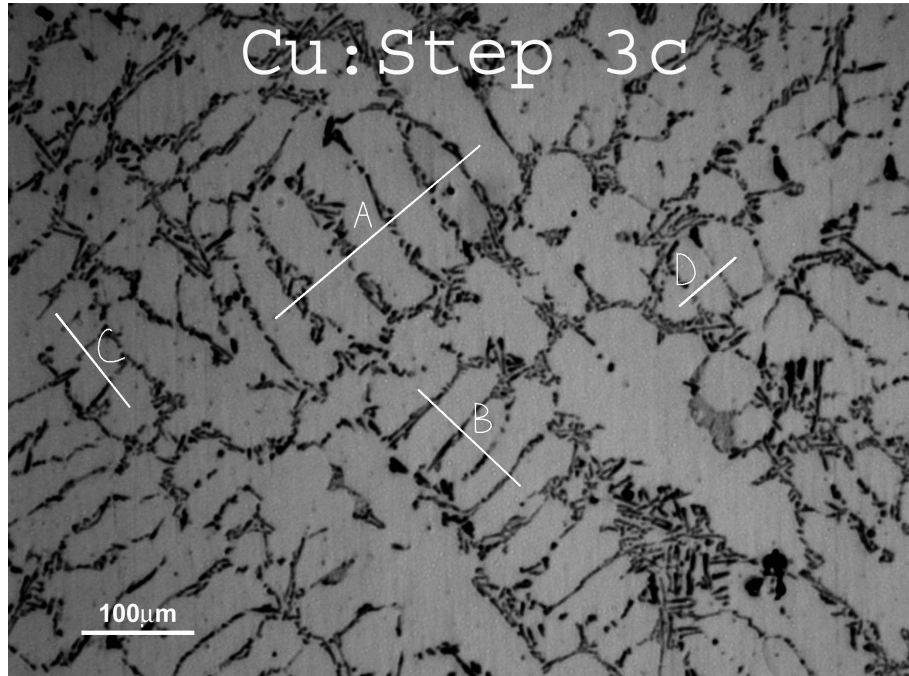


Figure 28: Measurements of SDAS in 3rd step of copper mold casting

Table 6: Total number of secondary dendrites measured

Casting	Step 1			Step 2			Step 3			Step 4			Total
	1	2	3	1	2	3	1	2	3	1	2	3	
Silica	28	49	55	22	50	41	35	53	41	21	36	35	466
Zircon	51	27	42	28	44	50	35	27	46	38	25	38	451
Copper	69	48	57	64	56	65	42	55	56	37	51	59	659

4. RESULTS AND DISCUSSION

4.1 Cooling Rate Comparison of Molds

As noted previously, one major disadvantage of ‘V’-process molding is its inability to cool castings as fast as its other sand molding counterparts. This has two separate negative consequences: (1) the production rate is lower because the cooling times are longer and (2) the mechanical properties are not quite as good because the SDAS is larger. One useful parameter to aid in determining which mold will have a higher cooling rate is the molds effective thermal conductivity. Thermal conductivity, k , provides an indication of the rate at which heat is transferred in a given material [23]. Values for the effective thermal conductivity obtained from Chiew and Glandt’s model, as explained in Section 4.2, for the silica sand, zircon sand, and copper particulate molds are given in Table 7.

Table 7: Thermal Conductivity of Casting Molds

	Silica Sand Mold	Zircon Sand Mold	Copper Particulate Mold
k , W/mK	0.327	0.336	0.433

The data of Table 7 suggest that a zircon sand mold should exhibit a slightly higher cooling rate as compared to a silica sand mold. More interesting though is that a copper particulate mold should have a significantly higher cooling rate than either silica or zircon sand molds.

Typical temperature profiles for an aluminum step casting in a silica sand, zircon sand, and copper particulate mold are shown in Figures 29, 30, and 31, respectively. The experimentally determined solidification times for nine different stepped-pattern aluminum castings made from three zircon molds, three silica molds, and three copper particulate molds are given in Tables 8, 9, and 10, respectively. The average solidification times of Tables 8, 9, and 10 are shown in the bar graph of Figure 32.

From the temperature profiles of the three molds, the copper particulate mold solidified much faster than either the silica or zircon sand molds. The zircon sand mold appears to solidify slightly faster than the silica sand mold. Figure 32 clearly shows that the castings in the copper particulate mold solidified much faster than the castings in the sand molds. The bar chart also shows that the two thickest steps of the castings in the zircon sand mold solidified slightly faster than the corresponding steps in the silica sand mold. Additional analysis of these data is required to discern the statistical significance, if any, of these apparent differences.

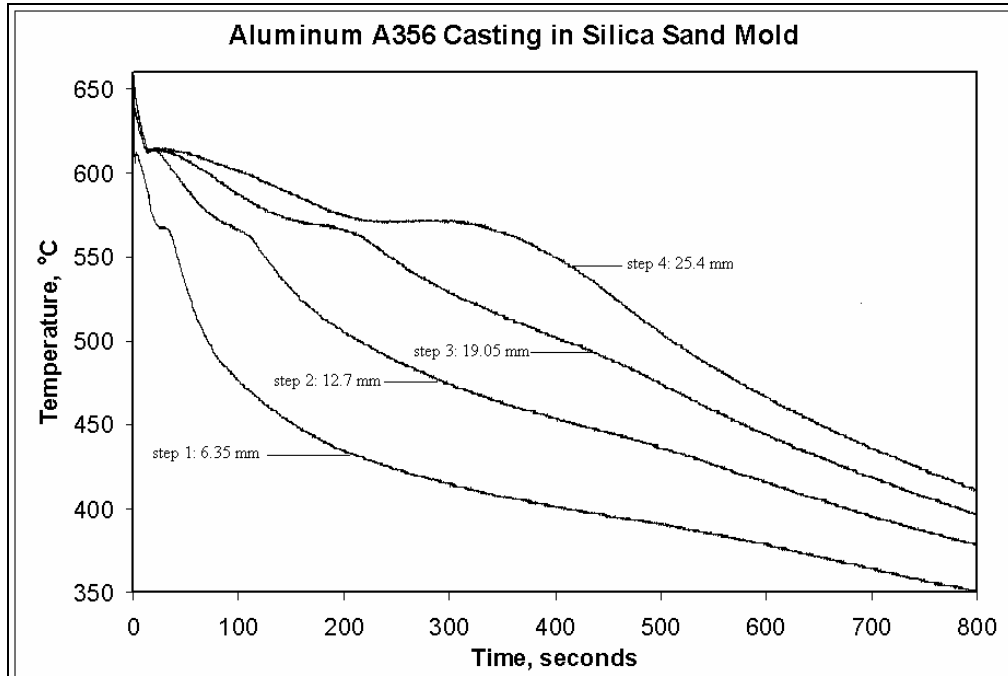


Figure 29: Temperature Profile of Aluminum A356 Cast Step Pattern in Silica Sand Mold

Table 8: Experimentally Determined Solidification Time in Seconds for 3 Aluminum A356.2 Castings in Silica Sand Molds

Silica Sand Mold Castings				
Casting	1	2	3	Average
step 1	33	33	34	33
step 2	104	81	95	94
step 3	194	172	194	187
step 4	296	287	314	299

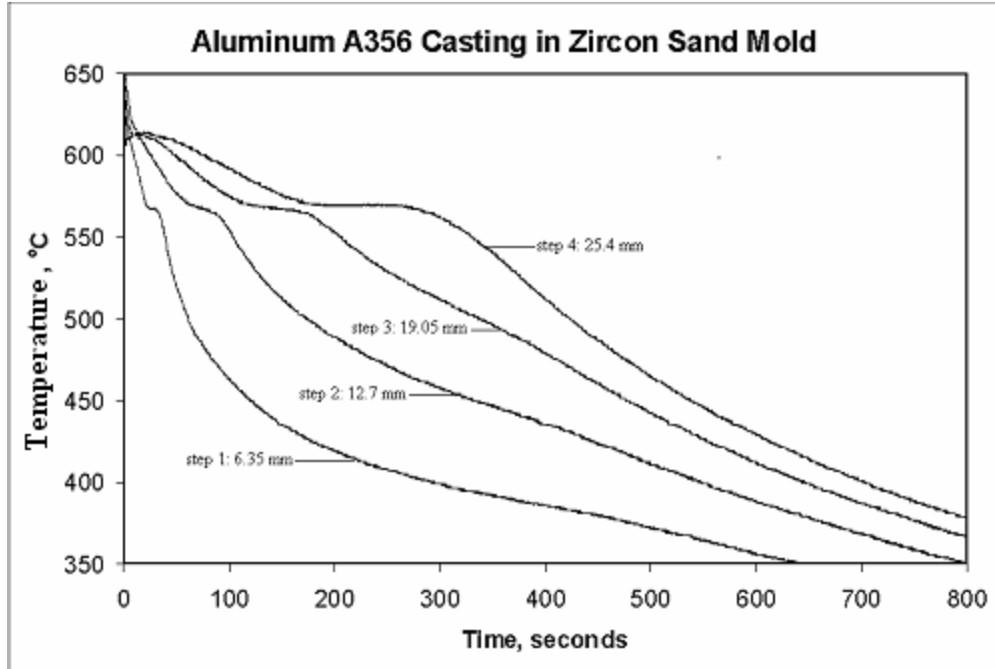


Figure 30: Temperature Profile of Aluminum A356 Cast Step Pattern in Zircon Sand Mold

Table 9: Experimentally Determined Solidification Time in Seconds for 3 Aluminum A356.2 Castings in Zircon Sand Molds

Zircon Sand Mold Castings				
Casting	1	2	3	Average
step 1	34	48	32	38
step 2	88	106	86	93
step 3	164	196	168	176
step 4	256	303	269	276

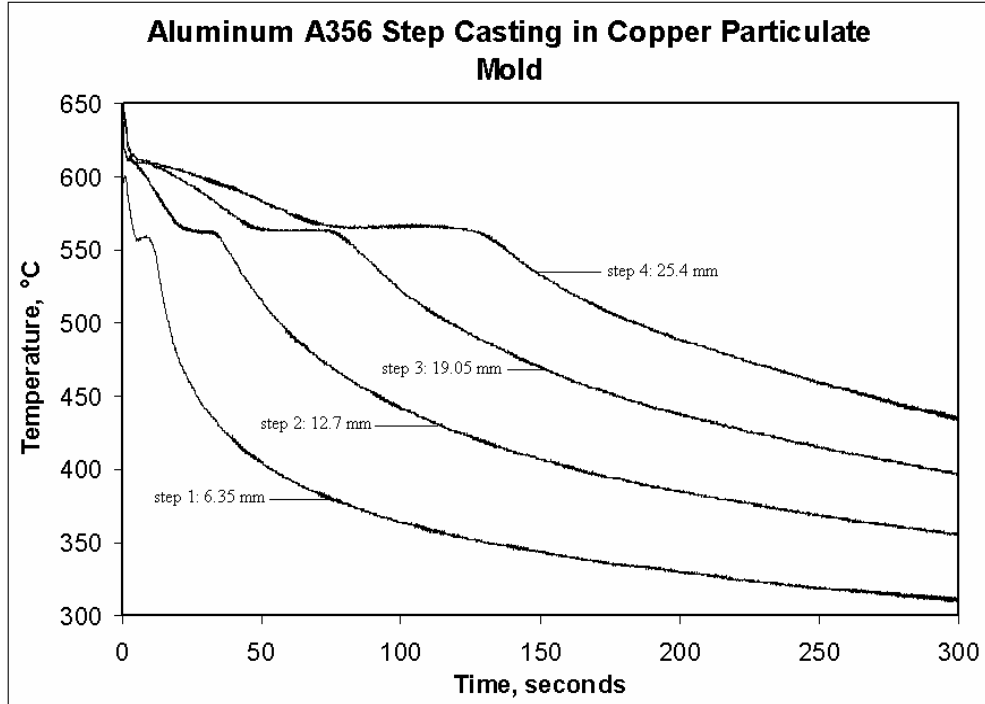


Figure 31: Temperature Profile of Aluminum A356 Cast Step Pattern in Copper Particulate Mold

Table 10: Experimentally Determined Solidification Time in Seconds for 3 Aluminum A356.2 Castings in Copper Particulate Molds

Copper Particulate Mold Castings				
Casting	1	2	3	Average
step 1	13	12	18	14
step 2	36	34	52	41
step 3	71	76	102	83
step 4	96	129	168	131

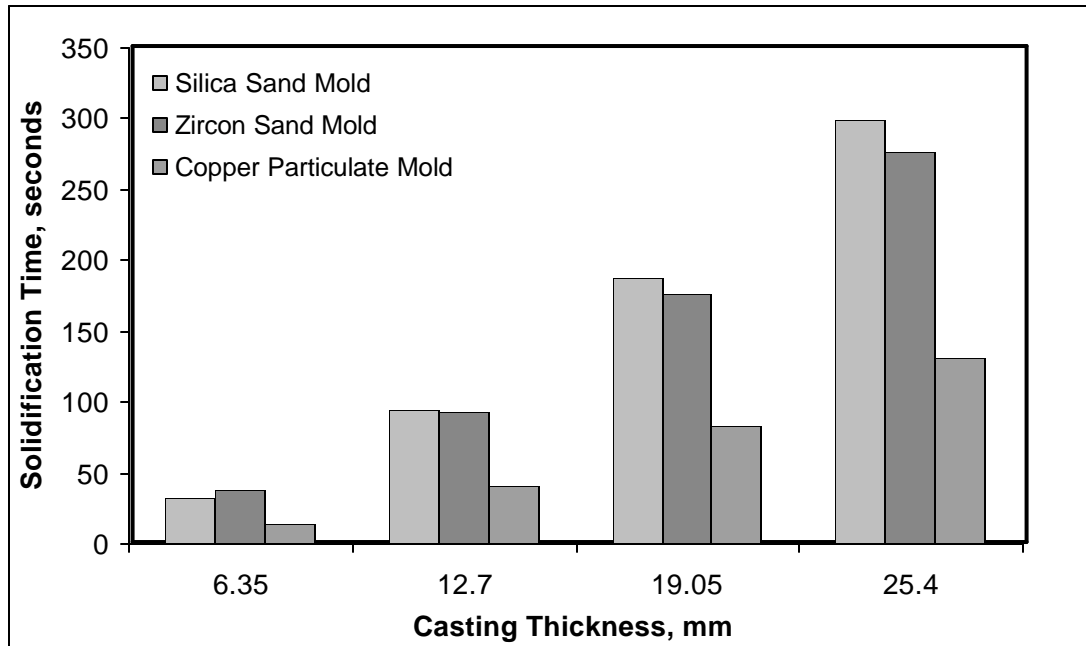


Figure 32: Graphical Representation of the Experimentally Determined Solidification Time as a Function of Step Thickness for the Three Mold Medias

To quantify the statistical significance between the observed differences in the cooling behavior between the molds, a one-sided analysis of variance (ANOVA) table was prepared to compare the solidification times between the corresponding steps of silica sand, zircon sand, and copper particulate molds. A statistically significant difference between two solidification times was accepted when the F_0 statistic was larger than the F_1 statistic at the 95% confidence level. Conversely, when the F_0 statistic was lower than the F_1 statistic, no significant difference was accepted between the two solidification times at the 95% confidence level. All F_0 statistics obtained from these tests are given in Table C-32 in Appendix C. The percent difference in the solidification times of the steps in the zircon sand and silica sand molds are shown in Table 11 and the

statistical significance results of the ANOVA test at the 95% confidence level are also given.

Table 11: Solidification Time Differences: Silica - Zircon Sand Molds

	% Difference ($t_f^{silica} - t_f^{zircon}$)	Significant at the 95% Level?
step 1	-13.50	No
step 2	0.25	No
step 3	5.88	No
step 4	7.90	No

As expected from the work of Murton and Buhr [5] and judging by the rate of heat the two molds could absorb, there is no significant difference between the cooling rate of aluminum in a silica sand or a zircon sand mold for the ‘V’ Process experiments conducted here. Although there is an apparent 13.5% increase in solidification time for the smallest steps in the zircon sand molds as compared to the silica sand molds, the larger zircon sand molded steps exhibit decreases in solidification times of 0.25, 5.88, and 7.90. Additional experimentation is required to establish whether the usage of silica versus zircon sands exhibit any real significant differences.

The results of the statistical comparison between the solidification times of the steps in silica sand molds and copper particulate molds are detailed in Table 12 and the zircon sand molds and the copper particulate molds in Table 13. As expected, the results indicate that there is a large decrease in solidification times for all steps when cast in the copper particulate molds and all differences are statistically significant at the 95% confidence levels.

Table 12: Solidification Time Differences: Silica Sand – Copper Particulate Molds

	% Difference ($t_f^{silica} - t_f^{copper}$)	Significant at the 95% Level?
step 1	79.30	Yes
step 2	78.79	Yes
step 3	76.92	Yes
step 4	78.04	Yes

Table 13: Solidification Time Differences: Zircon Sand – Copper Particulate Molds

	% Difference ($t_f^{zircon} - t_f^{copper}$)	Significant at the 95% Level?
step 1	90.38	Yes
step 2	78.58	Yes
step 3	71.85	Yes
step 4	71.24	Yes

4.2 Thermal Analysis – Theoretical Prediction of Solidification Times

Equation (2.6) enables prediction of the solidification time of a casting under the assumptions of (1) the mold is a semi-infinite medium, (2) solidification is governed by the removal of latent heat, and (3) the solidification temperature of the melt is a constant. A number of thermophysical properties and heat transfer parameters are required for the alloy being cast and the mold materials to apply Equation (2.6). The effective thermal conductivity (ETC) of the particular mold must be estimated. As discussed in the literature review, three different methods are available for estimating the ETC of a particulate mold. The requisite thermophysical properties and related parameters needed for estimation of the ETC are given in the Table 14.

Table 14: Values used for Effective Thermal Conductivity (ETC) Estimates

	ϵ	k_s , W/mK	β	α
Silica sand	0.396	1.4	0.909	1.183
Zircon sand	0.404	1.76	0.928	1.188
Copper part.	0.4	401	0.999663	1.186

ϵ was determined from the ratio between the measured density of the particulate with respect to the corresponding material's bulk density. Utilizing the values from Table 8 and setting k_l equal to 0.045 W/m K (i.e., the thermal conductivity of air at 300K [23]) enabled the effective thermal conductivity of the three mold materials to be estimated using the methodologies of Gori and Corasaniti [10], Peterson and Fletcher [11], and Chiew and Glandt [14]. The results of these calculations are summarized in Table 15. The estimated values for the effective thermal conductivities of the various mold materials are similar.

Table 15: Effective Thermal Conductivity Estimates

	k_e , W/mK			
	Gori and Corasaniti	Peterson <i>et al.</i> , max	Peterson <i>et al.</i> , min	Chiew and Glandt
Silica sand	0.234	0.863	0.108	0.327
Zircon sand	0.24	1.09	0.108	0.336
Copper part.	0.287	241	0.112	0.433

Equation (2.6) also requires geometric data for the casting being produced. The masses (m_f) and conduction heat transfer areas (A) of the various casting steps are shown in Table 16. Thermophysical properties of the molding particulates are given in Table 17 while Table 18 shows the thermophysical property data of the molten A356.2 aluminum alloy.

Table 16: Geometric Properties of the Cast Steps

	step 1	step 2	step 3	step 4
m_f , kg	0.109	0.219	0.328	0.438
A , m ²	0.0144	0.015	0.0156	0.0163

Table 17: Thermophysical Properties of the Mold Materials [24]

	$c_{p,m}$ J/kgK	ρ_m g/cm ³
silica sand	1183	1.6
zircon sand	837	2.72
copper part.	642	5.34

Table 18: Molten Aluminum Thermophysical Properties [24]

H_f	391 kJ/kg
T_s	943 K
T_i	296 K

The solidification times for a wide range of possible step thicknesses and the silica, zircon and copper molding materials were estimated using the estimated effective thermal conductivities of the molds. These theoretical predictions are compared to the experimentally determined solidification times of the discrete step thicknesses investigated in Figures 33, 34 and 35 for the silica sand, zircon sand and the copper particulate molds, respectively. Although the methodology of Peterson and Fletcher [11] to estimate the upper and lower limits of effective thermal conductivity (assuming parallel or serial heat transport, respectively) is useful for order of magnitude estimates, the more refined approaches of Gori and Corasaniti [10] and Chiew and Glandt [14] more accurately predict the solidification times in the current experiments. In fact, Chiew and Glandt's method appears to predict the observed solidification times quite well for all mold materials.

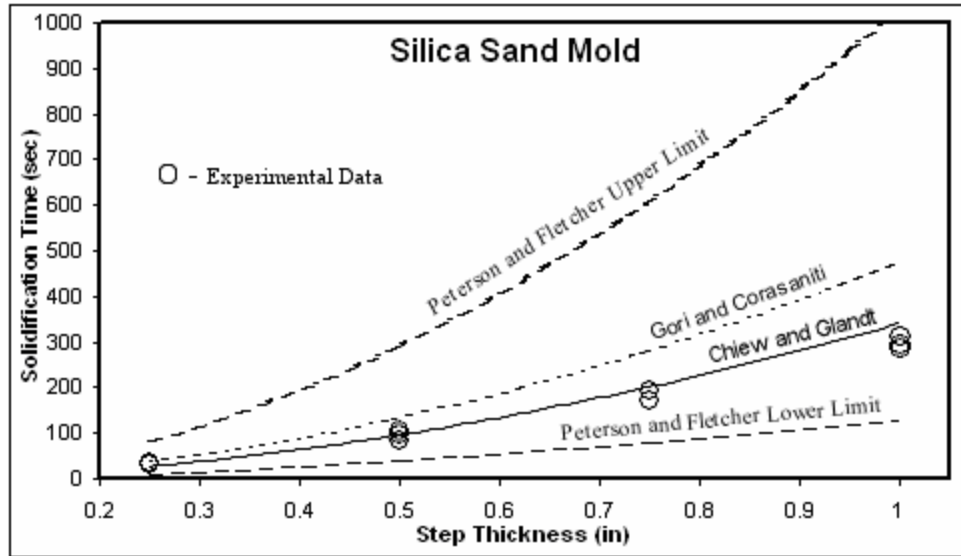


Figure 33: Comparison of Experimental and Theoretical Solidification Times for Aluminum A356.2 in a Silica Sand Mold

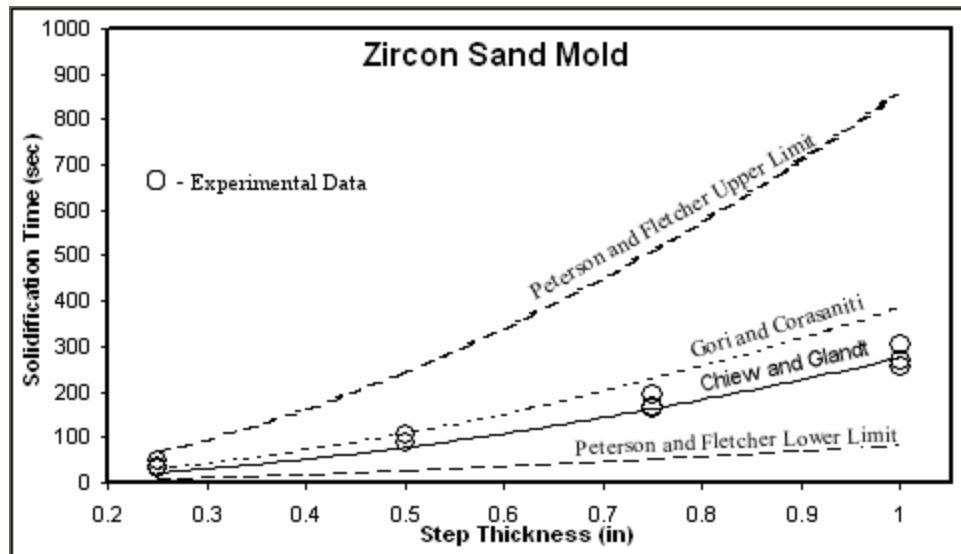


Figure 34: Comparison of Experimental and Theoretical Solidification Times for Aluminum A356.2 in a Zircon Sand Mold

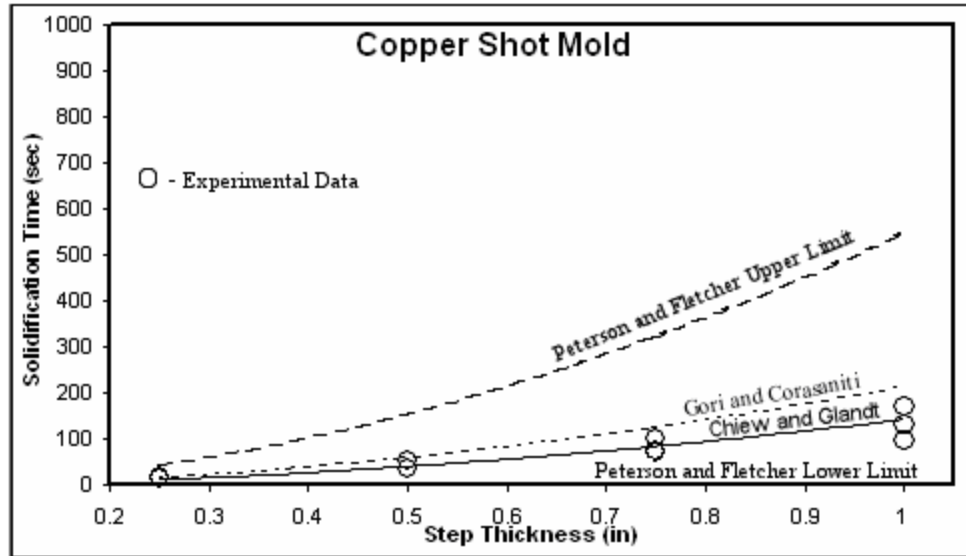


Figure 35: Comparison of Experimental and Theoretical Solidification Times for Aluminum A356.2 in a Copper Particulate Mold

The predicted solidification times for each step are presented in Table 19. One-way ANOVA tables between the experimentally observed solidification times for each step in each mold material and the corresponding theoretical predictions of solidification times using the methods of Gori and Corasaniti [10] and Chiew and Glandt [14] were then prepared to statistically test the two methods. As before, the F_0 statistics from the ANOVA tables were compared with the F_1 statistics. There was a significant difference between the theoretically determined solidification time and the experimentally determined solidification time if the F_0 statistic was larger than the F_1 statistic. There was no significant difference between the two if the F_0 statistic was lower than the F_1 statistic. Statistically significant differences between the experimental data and the theoretical predictions indicate that the theoretical prediction does not do a good job predicting the observed behavior at the 95% confidence level. All F_0 statistics created during this

analysis are listed in Tables C-33 and C-34 in Appendix C. Tables 20 and 21 display the results obtained from the statistical tests of the methods proposed by Gori and Corasaniti [10] and Chiew and Glandt [14], respectively. ‘No’ denotes no significant difference and ‘Yes’ denotes a significant difference between the experimentally determined solidification time and the theoretically determined solidification time.

Ten of the twelve steps display significant differences between the experimentally observed solidification times and the solidification times calculated using the ETC model of Gori and Corasaniti [10]. Conversely, nine of the twelve steps display no statistically significant differences between the experimentally observed solidification times and the solidification times calculated using Chiew and Glandt [14] ETC model. These results quantify the finding that Chiew and Glandt’s model for estimating the ETC of a packed bed provides the most accurate value for determining the time of solidification of castings in the present experiments.

Table 19: Predicted Solidification Times

		Solidification Time (seconds)			
ETC Method		Chiew	Gori	Peterson (Upper Limit)	Peterson (Lower Limit)
Silica	step 1	27	38	81	10
	step 2	99	138	297	37
	step 3	204	285	615	77
	step 4	334	467	1008	126
ETC Method		Chiew	Gori	Peterson (Upper Limit)	Peterson (Lower Limit)
Zircon	step 1	22	30	68	7
	step 2	80	112	249	25
	step 3	165	231	515	51
	step 4	270	379	844	84
ETC Method		Chiew	Gori	Peterson (Upper Limit)	Peterson (Lower Limit)
Copper	step 1	11	17	43	0.02
	step 2	41	62	158	0.07
	step 3	85	128	327	0.15
	step 4	139	210	536	0.25

Table 20: Statistics Comparing Gori and Corasaniti's ETC Model

	Silica Sand Mold	Zircon Sand Mold	Copper Particulate Mold
step 1	Yes	No	No
step 2	Yes	Yes	Yes
step 3	Yes	Yes	Yes
step 4	Yes	Yes	Yes

Table 21: Statistics Comparing Chiew and Glandt's ETC Model

	Silica Sand Mold	Zircon Sand Mold	Copper Particulate Mold
step 1	Yes	Yes	No
step 2	No	No	No
step 3	No	No	No
step 4	Yes	No	No

4.3 Secondary Dendrite Arm Spacing Measurements

As detailed in the Experimental Procedures, all SDAS were measured from micrographs taken from the corresponding position in each casting. To see the effect that solidification time has on the coarsening on secondary dendrites, four different micrographs, one from each step thickness of a casting, are shown in Figures 36-39. All micrographs were taken under the same magnification. Notice that as the thickness of each step increases, so does the width of the secondary dendrites. This is due to the thicker steps need to release more heat, therefore increasing its time of solidification.

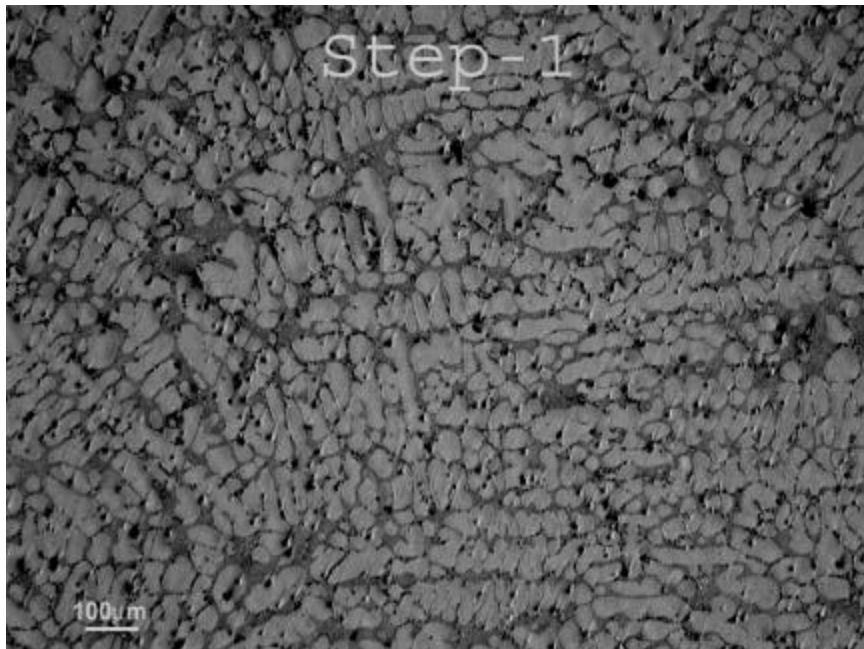


Figure 36: Micrograph of Secondary Dendrite Arms from a Step Thickness of 6.35mm

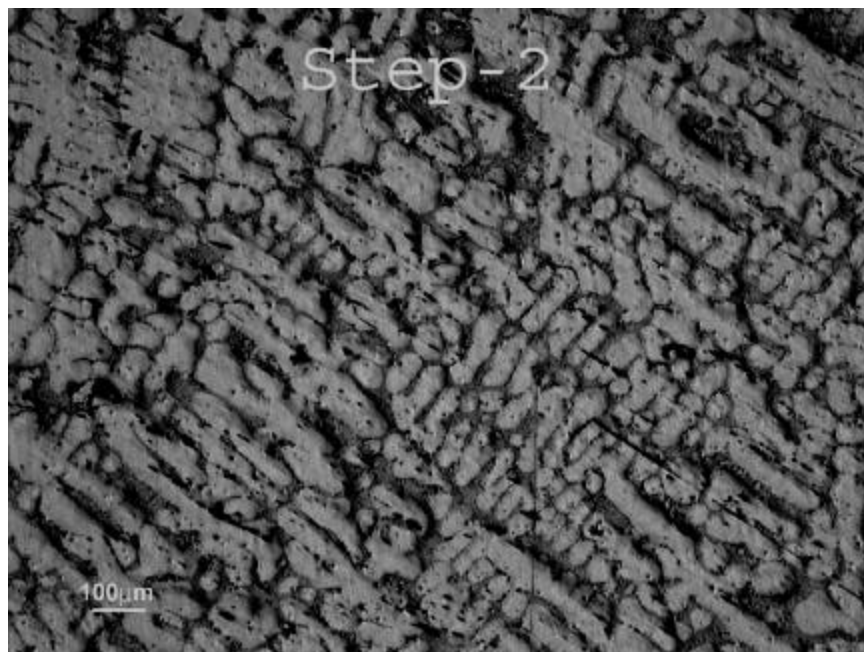


Figure 37: Micrograph of Secondary Dendrite Arms from a Step Thickness of 12.7mm

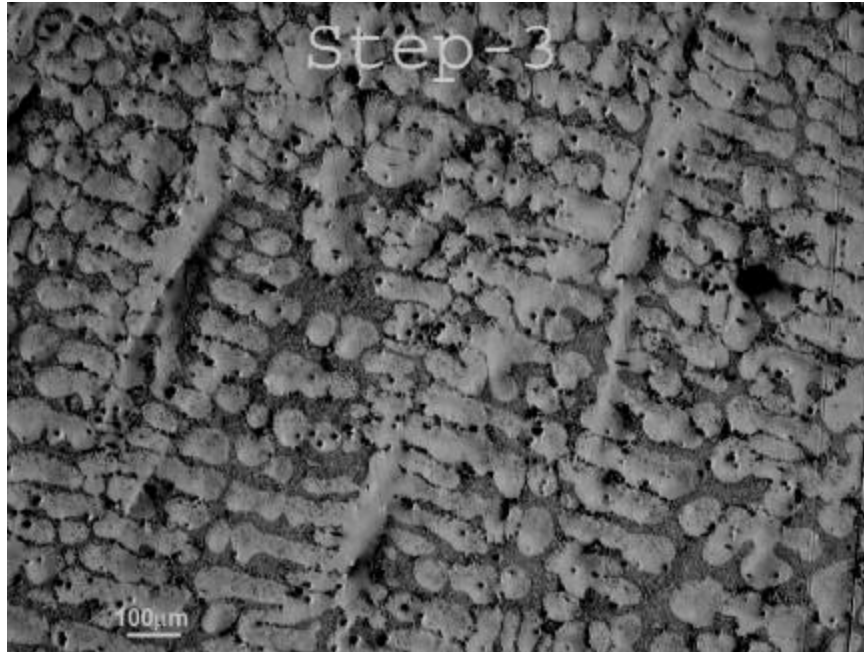


Figure 38: Micrograph of Secondary Dendrite Arms from a Step Thickness of 19.05mm

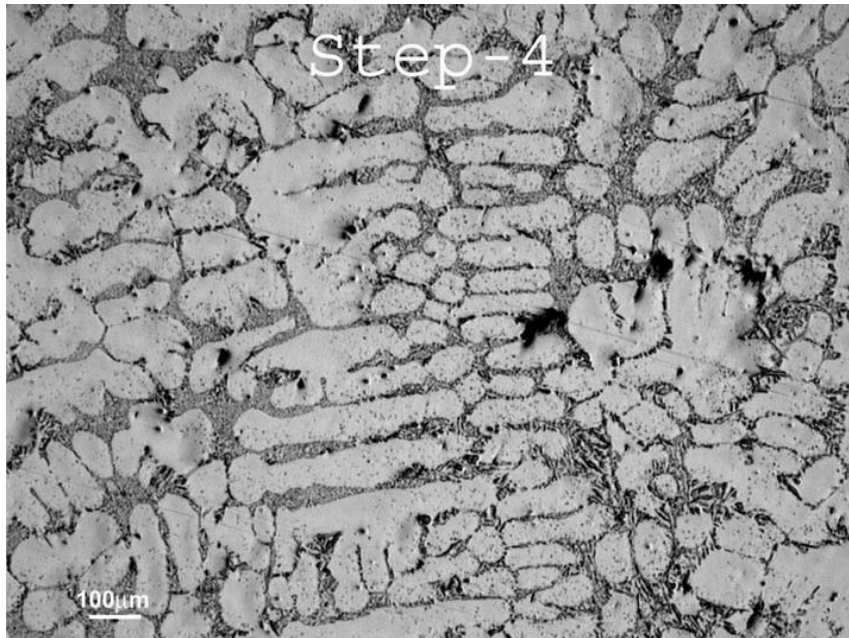


Figure 39: Micrograph of Secondary Dendrite Arms from a Step Thickness of 25.4mm

The measured SDAS from the micrographs of the aluminum castings in silica sand, zircon sand, and copper particulate molds are tabulated in Tables 22, 23, and 24. As mentioned, three castings from each of three molds were metallographically sectioned, mounted and characterized.

Table 22: Experimentally Determined SDAS for Silica Sand Mold

	SDAS (microns): Silica Sand Mold			
	Casting # 1	Casting # 2	Casting # 3	Average
step 1	35.1	53.3	44.6	44.3
step 2	47.5	68.4	59.4	58.4
step 3	46.4	80.6	70.4	65.8
step 4	67.2	102.1	113.4	94.2

Table 23: Experimentally Determined SDAS for Zircon Sand Mold

	SDAS (microns): Zircon Sand Mold			
	Casting # 1	Casting # 2	Casting # 3	Average
step 1	32.6	40.9	48.4	40.6
step 2	29.7	70.4	69.9	56.7
step 3	60.8	107.9	85.4	84.7
step 4	64.2	115.6	96.7	92.2

Table 24: Experimentally Determined SDAS for Copper Particulate Mold

	SDAS (microns): Copper Particulate Mold			
	Casting # 1	Casting # 2	Casting # 3	Average
step 1	17.0	18.7	25.4	20.4
step 2	26.5	30.3	49.3	35.4
step 3	38.8	40.1	41.1	40.0
step 4	48.4	53.5	51.6	51.2

The effective thermal conductivities in the silica sand, zircon sand, and copper particulate molds were used from Chiew and Glandt's model [14] to theoretically predict solidification times of aluminum A356.2 in the molds. These calculated solidification times were then used to estimate SDAS with Kirkwood's theoretical model [22] and the

three empirical models of Bamberger [20], Emadi and Whiting [19], and Spear and Gardner [18]. The estimated SDAS are shown in Tables 25, 26, 27, and 28. The constant A_{si} in Bamberger's model was determined to be $13.1\mu\text{m}/\text{s}^{0.43}$ by interpolating from the values given in Table 3 for aluminum with a 7 wt % silicon. For Kirkwood's model, the value of 'M' was chosen to be $5.43\mu\text{m}^3/\text{s}$ after the work of Peres et al. for aluminum with 7 wt % weight of silicon. The values used for the constants 'a' and 'C' in Emadi and Whiting's model are given in Table 2 for aluminum A356 and are $-0.3327\mu\text{m}/\text{s}/^\circ\text{C}$ and $1.808\mu\text{m}$, respectively.

The experimentally determined values for SDAS and the predictions of Tables 25-28 are plotted against cooling rate in Figure 40 and against solidification time in Figure 41. There is considerable scatter in the experimental data. The empirical models of Bamberger [20] and Emadi and Whiting [19] tend to over predict SDAS whereas the theoretical model of Kirkwood [22] tends to under predict SDAS. Spear and Gardner's [18] empirical model provides a reasonable mean value estimate for these data. A statistical analysis was performed between the four theoretical models and experimental data. The results of this analysis are given in Appendix D. From the statistical analysis, Bamberger's model doesn't appear to be an accurate model for predicting SDAS from the author's work. Only three out of twelve steps showed no significant difference in the theoretical and experimental SDAS. While Kirkwood and Emadi and Whiting's models fared slightly better than Bamberger's, neither accurately predicted the SDAS from the castings made. Both models only showed six of the twelve steps to have no significant difference in the theoretical and experimentally determined SDAS. Spear and Gardner's model showed only significant differences between the theoretical SDAS and

experimental SDAS in two of the twelve steps cast. Thus Spear and Gardner's model appears to be the most accurate model for the author's data.

Table 25: Predicted SDAS Using Bamberger's Empirical Model

	Bamberger: SDAS, microns		
Mold	Silica Sand	Zircon Sand	Copper Particulate
step 1	54.0	49.5	36.7
step 2	94.5	86.2	64.7
step 3	128.9	117.7	88.5
step 4	159.4	145.5	109.3

Table 26: Predicted SDAS Using Kirkwood's Theoretical Model

	Kirkwood: SDAS, microns		
Mold	Silica Sand	Zircon Sand	Copper Particulate
step 1	26.4	24.6	19.5
step 2	40.7	37.9	30.3
step 3	51.7	48.2	38.6
step 4	61.0	56.8	45.5

Table 27: Predicted SDAS Using Emadi and Whiting's Empirical Model

	Emadi and Whiting: SDAS, microns		
Mold	Silica Sand	Zircon Sand	Copper Particulate
step 1	53.1	49.6	39.4
step 2	81.8	76.2	61.0
step 3	104.0	96.9	77.7
step 4	122.5	114.2	91.5

Table 28: Predicted SDAS Using Spear and Gardner's Empirical Model

	Spear and Gardner: SDAS, microns		
Mold	Silica Sand	Zircon Sand	Copper Particulate
step 1	30.9	28.8	22.8
step 2	47.8	44.5	35.5
step 3	61.0	56.8	45.4
step 4	72.1	67.1	53.6

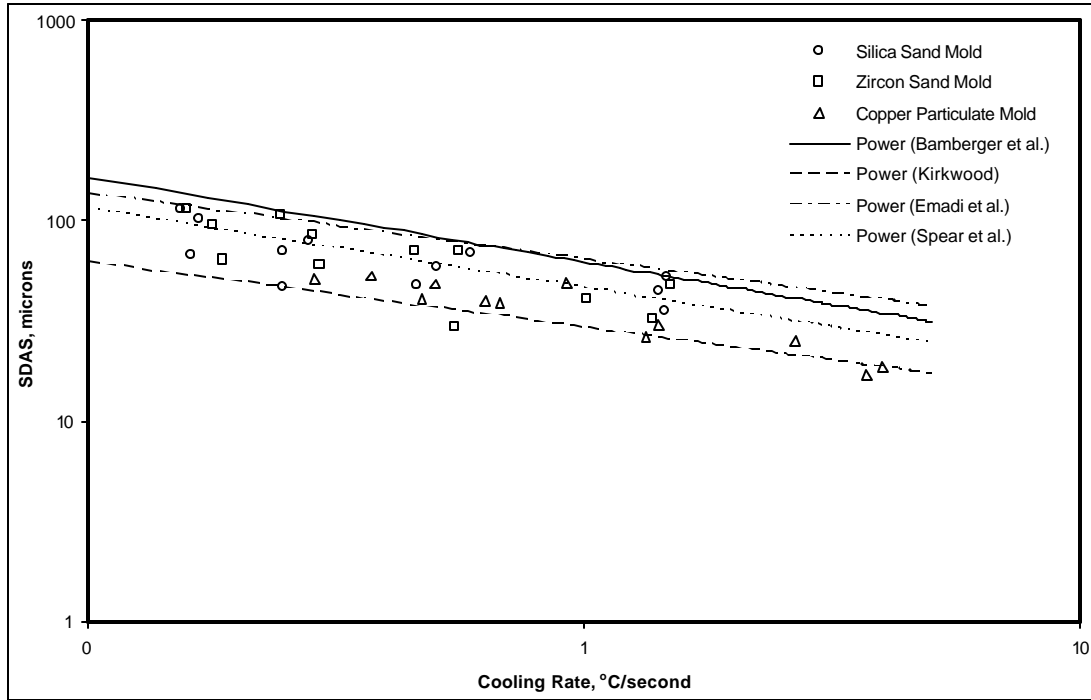


Figure 40: SDAS Data vs. Cooling Rate Comparison

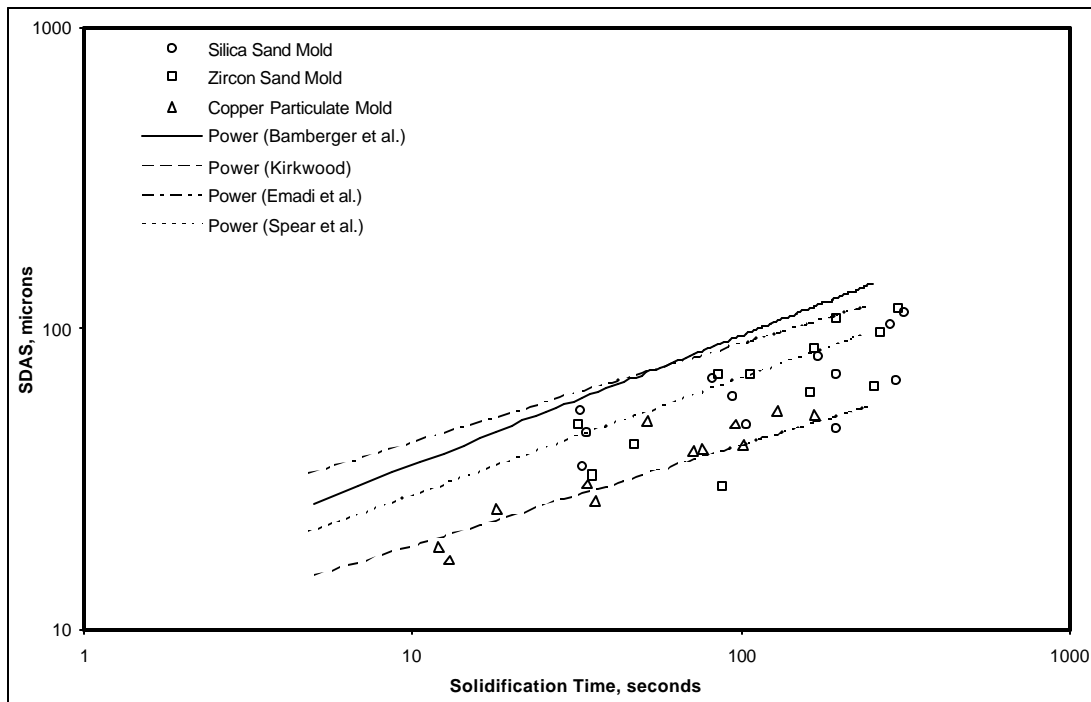


Figure 41: SDAS Data vs. Solidification Time Comparison

4.4 'V'-Process Development for a Complex Cored Casting

The 'V' Process offers a multitude of advantages for production of small production runs of metal prototype components. A small but complex valve plate component was chosen as a test case to develop 'V' Process casting procedures for aluminum parts that contain complex cored internal passageways. The valve plate chosen was 12 X 12 X 1.6 cm thick and contained a serpentine 'M' shaped cooling passage in the center of the plate.

4.4.1 Casting of a Cored Valve Plate in Aluminum A356.2 Alloy

Patterns for the upper mold (cope, Figure 42a) and the lower mold (drag, Figure 42b) were created using a Sanders Modelmaker II rapid prototyping machine at Auburn University. The two protrusions on the drag pattern are to secure the sand core and keep it from shifting horizontally. To obtain good surface detail in the cast components, the plastic film was heated longer and the vacuum was slowly applied to the carrier to prevent the vacuum from pulling a hole through the softened plastic film.

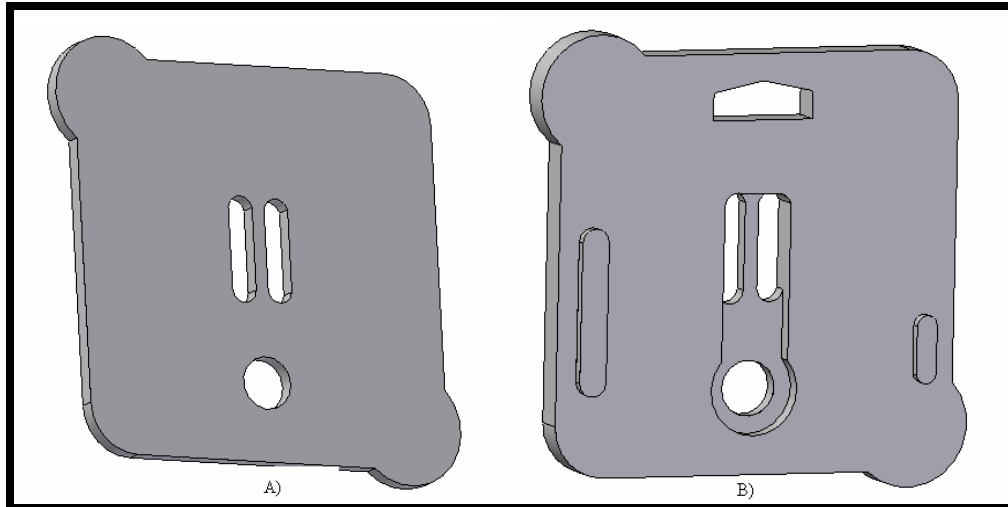


Figure 42: Cored Valve Plate Pattern for (a) Cope and (b) Drag

A sand core was chosen to create the hollow passageway inside the valve plate. Although silica sand was initially chosen for the sand core, zircon sand was found to perform better. All sand cores were produced in a Laempe laboratory sand core shooter using the phenolic-urethane-amine cold box process. The sand core was designed to have extensions on its left and right legs to provide openings in the final casting to provide an inlet and outlet in the component. In order to reliably place the sand core in the mold and maintain its position during casting, ‘C’ shaped chaplets were used at various locations to hold the sand core in place in the mold. The chaplets were made from the same alloy that was being used for casting. The chaplets were designed to melt in contact with the molten metal and become an integral part of the component. Eight chaplets were typically used to hold the position of the sand core; their positions are marked in Figure 43 by the black lines.

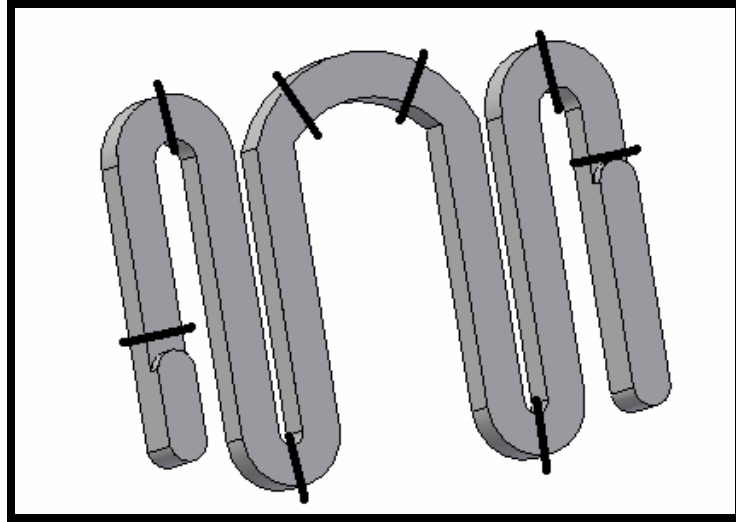


Figure 43: Chaplet Placement on Valve Plate Sand Core

When the core was set in the mold and the metal was poured, the chaplets would fuse into the solidifying metal during casting, leaving the sand core suspended in the casting. Unfortunately, the momentum of the entering molten metal would sometimes move the chaplets and allow the sand core to shift position. Also, if the molten metal was poured at too high of a temperature, the chaplets would melt before the liquid metal had begun to freeze and render the chaplets useless. To counteract these issues, protrusions were made in the prototyped pattern and sand core box at the airflow inlets and outlets. This caused a depression in the mold the exact size as the protrusions in the sand core, allowing the core to be inserted into the mold. This allowed for a consistent core setting method for each casting and eliminated the horizontal core shifts. For extra security, an industrial foundry paste was inserted inside the mold depressions so the sand cores legs would stick to the mold. However, the sand core was only secured at both ends and not in the middle. The middle of the low-density silica sand core could sometimes float upward sometimes

reaching the surface of the casting. Producing the cores with higher density zircon sand was found to improve this problem. A couple of chaplets were placed in the center of the sand core to hold its position vertically. This method of sand core placement allowed for the successful casting of the cored valve plate. Figure 44 shows a prepared drag mold for the cored valve plate including sand cores while Figure 45 shows the cope flask placed over the plastic film, which is drawn over the cope pattern.

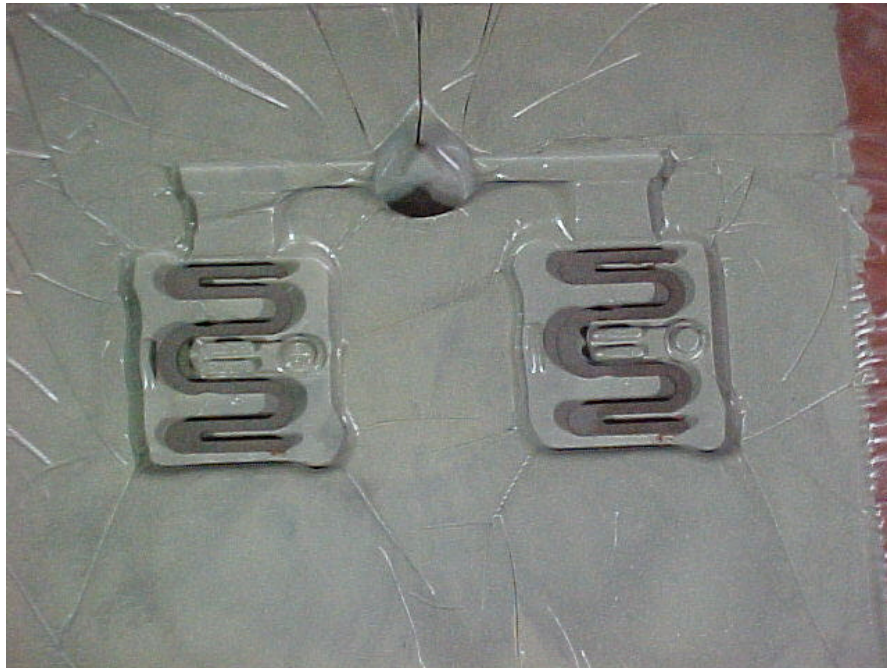


Figure 44: A Prepared Drag Mold with Sand Cores for Two Cored Valve Plates

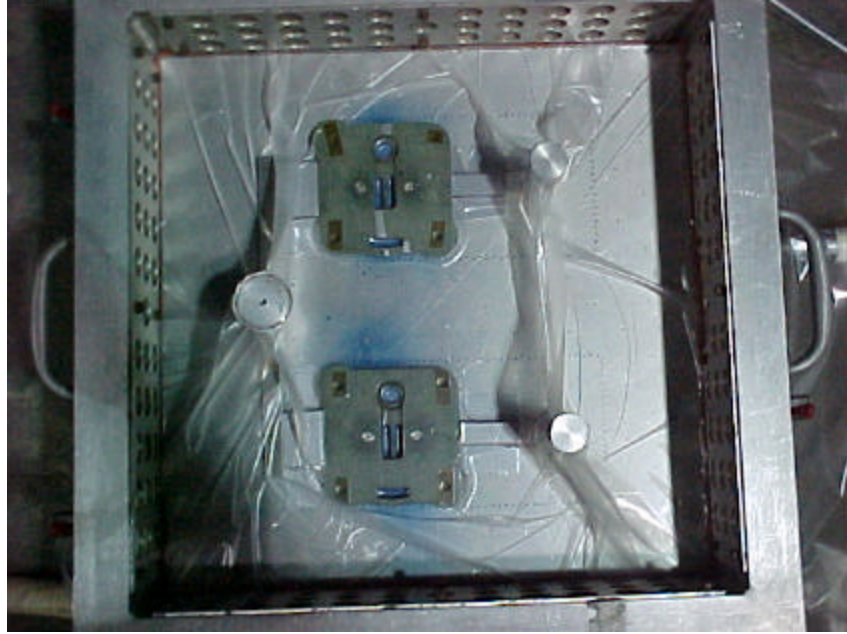


Figure 45: Plastic Film Formed Over Cope Pattern of Two Cored Valve Plates

By following the procedures outlined above, more than 50 cored valve plate castings were successfully produced from A356.2 aluminum alloy. Examples of such components are shown in Figures 46 and 47.



Figure 46: Post-Casting Aluminum A356.2 Cored Valve Plate



Figure 47: Post-Surfacing Aluminum A356.2 Cored Valve Plate

4.4.2 Casting of the Cored Valve Plate in Magnesium AZ91 Alloy

As mentioned previously, all metals were thought to be able to be cast in 'V' Process molds with the exception of magnesium, due to its low thermal heat content and its high chemical reactivity.

Before attempting to cast magnesium in a 'V' process mold, a standard operating procedure was prepared to safely avoid all potential hazards. See Appendix B. Because of magnesium's volatility, a special crucible was designed for the usage of 99%CO₂+1%SF₆ cover gas. This cover gas was blown over the molten magnesium, at a rate of 0.3 l/min, where it settled over the top of the melt, separating the melt from the atmosphere. In addition, the silica sand used for magnesium casting (molds and cores) contained 1% by volume of 50% potassium fluoroborate and 50% sulphur inhibitor to suppress and burning reactions. The same methods described above to place the sand cores were also used to make magnesium valve plates. However, instead of using chaplets made from aluminum A356.2, the chaplets were made from magnesium AZ91E. Once the molten magnesium had reached 760°C, the mold was flushed with SF₆, and the magnesium was poured into the mold. Figure 48 shows two successful valve plates made from magnesium.

In addition to the casting of magnesium valve plate components, magnesium castings were also prepared using the stepped patterns. The temperature profile of steps 1, 2, 3, and 4 with thicknesses of 6.35, 12.7, 19.05, 25.4 mm, respectively, is shown in Figure 49.



Figure 48: Final Magnesium Cast of Brake Valve Plates

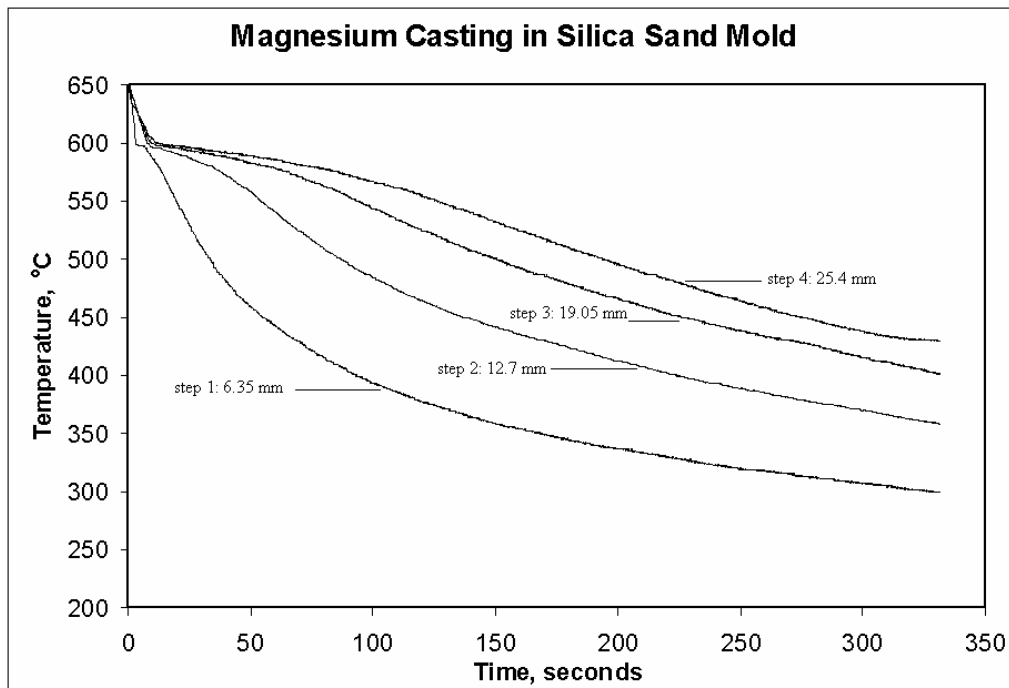


Figure 49: Temperature Profile of Magnesium AZ91 Cast Step Pattern in Silica Mold

5. SUMMARY AND CONCLUSION

5.1 Cooling Rate Comparison of Molds

In an attempt to decrease the solidification time of aluminum A356.2 using 'V' Process molding, three different mold medias (silica sand, zircon sand, and copper particulate) with different thermal properties were used to produce step castings with volumes of 41 cm³, 82 cm³, 123 cm³, and 164 cm³. A statistical analysis showed no significant difference at a 95% confidence level in the solidification times between the silica and zircon sand molds. However, the analysis showed a significant difference at a 95% confidence level in the solidification time between the copper particulate molds and both the silica and zircon sand molds. The copper mold decreased the solidification time of aluminum A356.2 by a factor of two or more over the silica and zircon sand molds.

5.2 Theoretical Prediction of Solidification Times

Before experimentally casting the steps in the silica sand, zircon sand, and copper particulate molds, an attempt was made to theoretically predict the solidification times of each step in each mold media. The effective thermal conductivities of each mold were estimated using methods proposed by Chiew and Glandt [14], Gori and Corasaniti [10], and Peterson and Fletcher [11]. These estimates with assumptions of semi-infinite solid for the mold and constant surface temperature for the solidifying metal allow Chvorinov's equation to be used to estimate the solidification time. Chiew and Glandt's

model of effective thermal conductivity [14] enabled the most accurate prediction of the solidification times for all mold media and casting thickness in the current experiments.

5.3 Theoretical Prediction of Secondary Dendrite Arm Spacings

The predicted solidification times obtained from using Chiew and Glandt's ETC model [14] were also used to predict the secondary dendrite arm spacings of each step in each of the three molds. Four models of dendrite arm spacing from the literature (Kirkwood [22], Bamberger [20], Emadi and Whiting [19], and Spear and Gardner [18]) were tested against the experimental results. Spear and Gardner's model [18] provided the best fit to the data.

5.4 Cored Valve Plate

Two primary obstacles existed when initially casting the aluminum A356.2 valve plates. Firstly, the ability to accurately transfer the intricacies of the valve plate into the mold. This obstacle was overcome by using a rapid prototyped pattern and controlling the level of vacuum applied when forming the plastic film on the pattern. Secondly, methods had to be developed to suspend the serpentine 'M' shaped sand core within the valve plate and prevent horizontal and vertical core shift. Vertical core shift was prevented by inserting chaplets on the sand core. The chaplets were constrained on the top and bottom by the mold walls. Once the molten metal was poured into the mold, the chaplets would fuse into the cast metal. Horizontal core shifting was prevented by the placement of the sand core's leg extensions into depressions created in the drag mold. By overcoming these issues, more than 50 valve plates were successfully cast.

Magnesium AZ91E was also used to cast the brake valve plate. In addition to the above issues, magnesium introduced several more complexities. Because of its high chemical volatility, a standard operating procedure was prepared to safely avoid all potential hazards. A special purpose crucible was designed that allowed for the flow of 99%CO₂+1%SF₆ cover gas to safely contain the molten magnesium. Also, inhibitors were added into the sand used for mold formation as another precautionary measure to prevent the molten magnesium from combustion. By following the standard operating procedures, successful valve plates and step castings were made in a 'V' Process mold using magnesium AZ91E.

6. FUTURE RESEARCH

Due to the high density and cost of copper, calculations were made to predict the solidification time of an aluminum casting in a steel particulate mold. The results showed very little difference with those from castings in the copper particulate mold. Therefore, experiments should be performed to determine a lighter and cheaper metallic particulate that would be practical in today's foundries. Also, due to the application of the plastic film onto the cope and drag in 'V' Process molding, the process is not easily automated. Research should be performed to determine a quicker and easier method of sealing the mold, such as a spray on polymer. A better understanding of the process can be achieved by the characterization of the vaporization of the plastic film when in contact with the molten metal. Perhaps with the addition of certain heat extracting elements in the plastic film, a higher cooling rate could be achieved.

REFERENCES

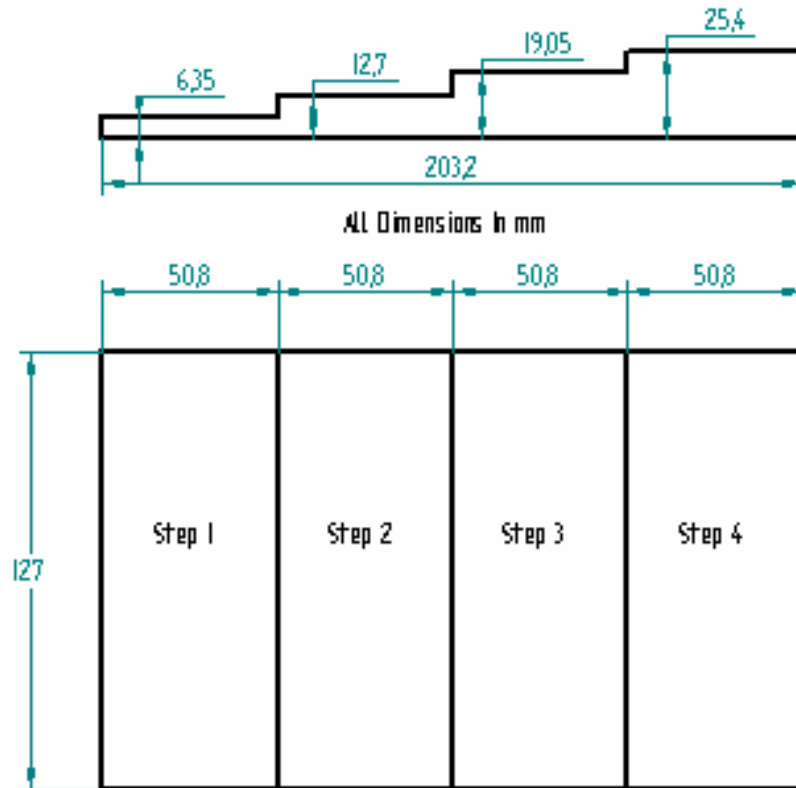
1. Kotzin E.L., *Metalcasting and Molding Processes*. AFS Publication, 1981.
2. Gouwens P.R., *Vacuum Molding (The V-Process): Perspective and Into the Future*. AFS Transactions 98-174.
3. Kaiser Aluminum and Chemical Sales Inc., *Casting Kaiser Aluminum*.1956, Chicago: 1st ed.
4. Cole G., Agarwal-Finstad R., and Grebetz J.C. *The potential for magnesium in the automotive industry*. Proc. 52nd Ann. World Magnesium Conf, 1995. p. 1-5.
5. Murton A.E., Buhr R.K., *An Evaluation of the Vacuum Molding Process*. AFS Transactions, 1976. 47: p. 43-48.
6. Flemings M.C., *Solidification Process*.1974, McGraw-Hill.
7. Campbell J., *Castings*.2003, Oxford: 2nd ed., Butterworth-Heinemann.
8. Chvorinov N., *Giesserei*, 1940. 27: p. 201-208.
9. Trbizan K., *Casting Simulation*. World Foundry Organization, 2001. paper 4: p. 83-97.
10. Gori F., Corasaniti S., *Theoretical Prediction of Soil Thermal Conductivity at Moderately High Temperatures*. Journal of Heat Transfer, 2002. 124: p. 1001-1008.
11. Peterson G.P., Fletcher L.S., *Effective Thermal Conductivity of Sintered Heat Pipe Wicks*. Journal of Thermophysics, 1987. 1: p. 343-347.

12. Maxwell J.C., *A Treatise on Electricity and Magnetism*.1873, Oxford: Vol. 1, Clarendon Press.
13. Gonzo E., *Estimating Correlations for the Effective Thermal Conductivity of Granular Materials*. Chemical Engineering Journal, 2002. 90: p. 299-302.
14. Chiew Y.C., Glandt E., *The Effect of Structure on the Conductivity of a Dispersion*. Journal of Coll. Interf. Science, 1983. 94: p. 90-104.
15. Reed-Hill R.E., Abbaschian R., *Physical Metallurgy Principles*.1994, Boston: 3rd ed., PWS Publishing.
16. Miguelucci E., AFS Transactions, 1985. 93: p. 913-916.
17. Jefferies Z., Archer R.S., *The Science of Metals*.1924, McGraw-Hill.
18. Spear R.E., Gardner G.R., *Dendrite Cell Size*. AFS Transactions, 1963. 71: p. 209-215.
19. Emadi D., Whiting L., *Determination of Solidification Characteristics of Al-Si Alloys by Thermal Analysis*. AFS Transactions, 2002. 110: p. 285-296.
20. Bamberger M., Weiss B.Z., Stupel M.M., *Heat flow and dendritic arm spacing in chill-cast Al-Si alloys*. Materials Science and Technology, 1987. 3: p. 49-56.
21. Peres M.D., Siqueira C.A., Garcia A., *Macrostructural and microstructural development in Al-Si alloys directionally solidified under unsteady-state conditions*. Journal of Alloys and Compounds, 2004. 381: p. 168-181.
22. Kirkwood D.H., *A simple model for dendrite arm coarsening during solidification*. Materials Science and Engineering, 1985. 73: p. L1-L4.
23. Incropera F. P., *Fundamentals of heat and mass transfer*.1985, New York: 2nd ed., Wiley.

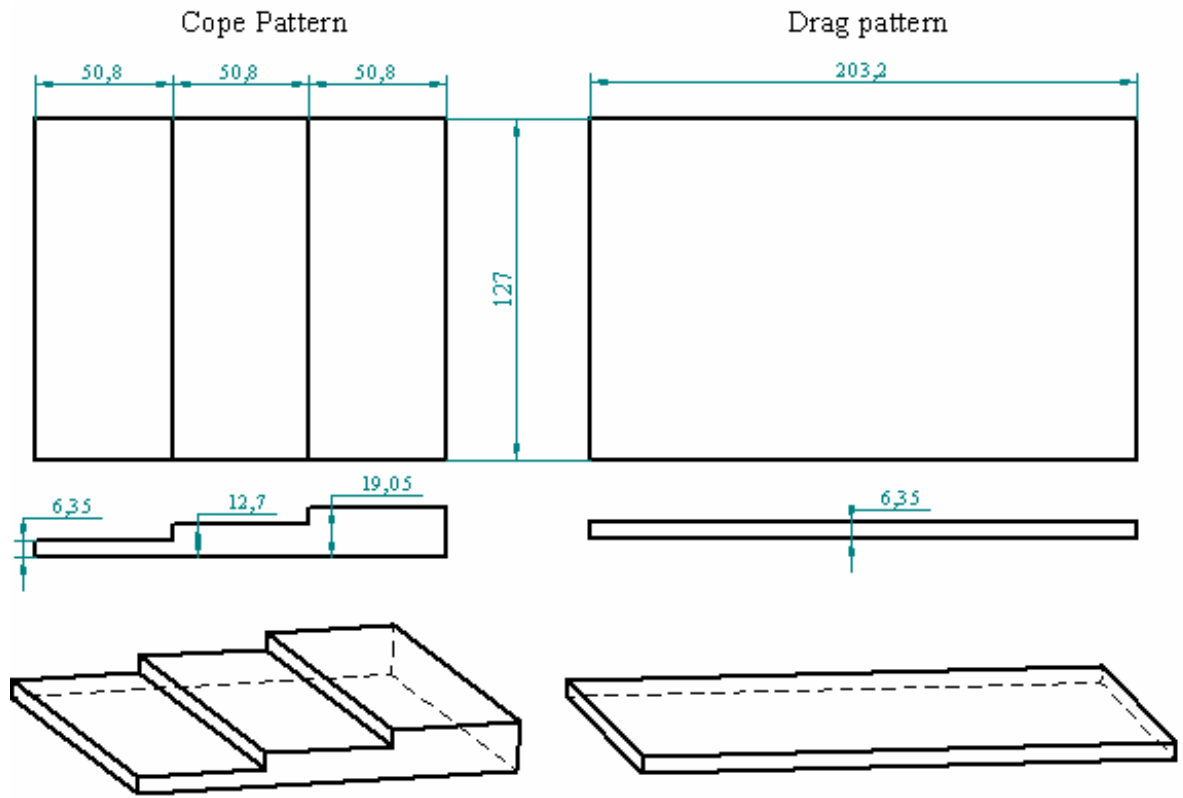
24. Poirier D.R., Poirier E.J., *Heat Transfer Fundamentals for Metal Casting*.1992,
Warrendale: The Minerals, Metals, & Materials Society.

Appendix-A

Detailed View of Step Casting Pattern



Detailed View of Step Pattern's Cope and Drag



All Dimensions in mm

Appendix-B

Standard Operating Procedures for Melting and Casting Magnesium

- 1) Lepel Furnace: The Lepel furnace is a 50 kW furnace used to melt metal by alternating electrical current through copper induction coils.
 - A) Before operating the furnace become familiar with controls and how to properly turn the Lepel on and off.
 - B) Before turning furnace on ensure that:
 - i. there are no water leaks.
 - ii. no conductive materials are within 5 feet of induction coils.
 - iii. the ceramic wool, lining the induction coils, is not worn. If it is then cut another piece and replace.
 - iv. the bricks, which the crucible is mounted on, are sturdy and are not cracked. If so, ensure that the Lepel is off and replace the bricks.
 - C) Never leave the Lepel unattended while it is in operation.
 - D) If any abnormal fumes or odors are emitted from the crucible, turn RF power off and exhaust the fumes or odors with the provided exhaust system.
 - E) If ANYTHING seems abnormal during operation of Lepel, turn RF power off immediately and consult your supervisor.

- 2) Storage and Handling: All magnesium, either it be an ingot or casting form, should be held in a noncombustible building and separated from other combustible materials.

Magnesium casting is to be cut from gating with a handsaw. The casting is to be cut in the designated area in Shop Building 3, which will be continuously cleaned in order to ease the task of gathering the magnesium chips and particulate. Once the particulate is gathered, it is to be placed into a metal container with tight fitting lid, which will be provided and labeled "Magnesium Particulate". Magnesium ingot is to be cut using band saw located in Shop Building 3.

The band saw and magnesium particulate should be cleaned after every use as described above.

Once the container holding the magnesium particulate is approximately three-fourths full, the container should be labeled with a “waste chemical” tag. Safety and Environmental Health, 4-4805, should then be called to pick up the container. For any questions regarding pick-up or storage, refer to “Safety and Environmental Health: Chemical Waste Management” booklet, chapters 2 and 3.

- 3) Molten Metal Testing: Magnesium alloy is a combustible metal due to its ease of ignition when it reaches a high specific area ratio. Pure magnesium has an ignition temperature of 623 °C (1153 °F), which is just below its melting temperature. However, for alloys and smaller parts, the ignition temperature could be considerably lower. While large castings do not present much of a threat of combustion, magnesium in the form of thin sections, fine particles, and in its molten state can present an ignition hazard. Extreme caution should be used when handling molten magnesium.
- A) The steel crucible, as opposed to the graphite crucible, is to be used when melting magnesium in the Lepel furnace. It was specifically designed with cover gas capability for magnesium melting (see 3.C below).
 - B) Ensure, before placing the magnesium in the crucible, that there are no cracks, moisture, or any form of debris (i.e. rust or any oxide layer, sand, or alumina wool.)
 - C) In order to prevent the molten bath surface from oxidizing, a mixture of 99% CO₂ and 1% SF₆ at a rate of 0.3 l/min will be continuously injected over the molten bath. This gas will completely cover the bath and separate it from the surrounding air by forming a surface film of MgO and MgF₂.
 - D) Also, as an additional precaution, sulfur can be used as a melting flux to aid in the separation of the molten bath from the atmosphere. The sulfur can be sprinkled over the top of the molten magnesium, where it will burn providing a cover gas of SO₂.
 - E) When near the molten metal, always wear:
 - i. Protective heat resistant clothing provided in lab. This includes a coat, britches, and shoe guards.

- ii. Protective heat resistant gloves, only.
- iii. Full face guards with safety glasses.
- iv. NEVER wear open-toe shoes.

- F) NEVER ALLOW ANY MOISTURE TO REACH MOLTEN METAL!!!
- G) When placing objects (i.e. additional metal, degasser, etc.) into molten metal, hold above molten metal for 15 seconds with iron tongs and slowly submerge the object into the liquid metal.
- H) When performing metallurgical tests in the molten magnesium (i.e. measuring temperature, inserting additional metal, degassing, taking porosity samples, or anything involving removing the crucible cover and inserting anything into the metal) always turn RF dial to 0 % and RF power off from the Lepel.
- D) If the molten bath begins to oxidize and ignite, sprinkle the sulfur flux over this area to extinguish the flame.
- J) Inspect all tools to be placed in contact with molten metal and clean ANY debris that may be on the tool. In addition, preheat all tools prior to contact with the molten metal.
- K) Food and drinks are strictly prohibited within lab area.

2) Transfer of Molten Metal From Crucible to Mold

- A) Ensure that the correct clothing is being worn as described in 2E of this document
- B) Ensure that there are no obstructions in your path from the furnace to the mold.
- C) When pouring molten magnesium into mold, use the provided exhaust fan to transport all fumes and gases outside the building.

3) In Case of Magnesium fire

- A) If in crucible:
 - i) If the molten bath begins to oxidize and a flame initiates, sprinkle the sulfur flux over this area to extinguish the flame.

- ii) If flame growth continues after application of the powder sulfur, immediately shut down the Lepel and extinguish the flame by sealing the crucible with cover to deprive the flame of oxygen.
- iii) using a METAL FIRE RATED FIRE EXTINGUISHER ONLY!!! Never use water/halogenated extinguishing agents.
- iv) If the flame remains after treatment with the METAL FIRE RATED FIRE EXTINGUISHER.
- v) Turn on the foundry area ventilation system to exhaust the fumes and particulate generated.

B) While transporting the molten magnesium from the crucible to the mold:

- i) If a spillage occurs during transport to the mold, cover the molten metal with dry sand + 1% potassium fluoborate inhibitor mixture. Spray it with METAL FIRE RATED FIRE EXTINGUISHER (if needed).
- ii) The mold will be contained in 4 X 3 feet sand box when pouring occurs. As in 3.b.i, if magnesium ignition occurs around the mold, cover with dry sand and spray with METAL FIRE RATED FIRE EXTINGUISHER (if needed).
- iii) Turn on the foundry area ventilation system to exhaust the fumes and particulate generated.

4) Post-Pouring

- A) Once the mold is filled, pour the remaining magnesium into to the iron crucible provided. Immediately, sprinkle the sulfur flux over the surface of the metal. Continue to add the sulfur as needed to prevent magnesium ignition.
- B) Sprinkle the sulfur flux over the mold onto the two risers and the sprue, where the metal is exposed to the atmosphere.
- C) Turn on the foundry area ventilation system to exhaust the SO₂ fumes generated.

3) Emergency Phone Numbers

- A) Police, Fire, and Rescue: 9-911 (accidents, spills)
- B) Safety and Environmental Health: 4-4870

Appendix-C

F₀ Statistics

Table C-29: F₀ Values from Statistical Comparisons between Mold Solidification Times

	F ₀ Values		
molds compared	Silica Sand Zircon Sand	Silica Sand Copper Particulate	Zircon Sand Copper Particulate
step 1	0.99	98.7	21
step 2	0	37.06	37.91
step 3	0.73	73.4	44.88
step 4	2	56.77	33.47

Table C-30: F₀ Values from Statistical Comparison between Predicted Solidification Time, Obtained from Chiew and Glandt's Model [14] for ETC Estimation, and Experimentally Determined Solidification Time.

	F ₀ Values		
molds	Silica Sand	Zircon Sand	Copper Particulate
step 1	257.33	11.02	3.23
step 2	0.7	4.35	0
step 3	5.49	1.22	0.04
step 4	20.07	0.18	0.15

Table C-31: F₀ Values from Statistical Comparison between Predicted Solidification Time, Obtained from Gori and Corasaniti's Model [10] for ETC Estimation, and Experimentally Determined Solidification Time.

	F ₀ Values		
molds	Silica Sand	Zircon Sand	Copper Particulate
step 1	158.08	2.74	2.06
step 2	46.02	8.61	14.03
step 3	177.94	29.98	21.93
step 4	453.36	54.47	14.41

Appendix-D

Statistical Analysis between SDAS Prediction Models

The abilities of the three empirical models and the theoretical model of Kirkwood to predict SDAS were analyzed statistically using one-sided ANOVA. Each step from each mold was compared in this analysis. The F_0 statistics obtained from the ANOVA tables were compared with the F_1 statistic. If the F_0 statistic was greater than the F_1 statistic then there was an indication of significant difference and if the F_0 statistic was lesser than F_1 , there was an indication of no significant difference. The results from the tests are tabulated below in Tables D-32, D-33, and D-34. In the tables, the letter ‘N’ signifies that there is no significant difference and the letter ‘S’ signifies that there is a significant difference between the compared theoretical and experimental SDAS.

Table D-32: Statistical Comparison Between Theoretical and Experimentally Determined SDAS For Silica Sand Molds

Silica Sand Mold	Model	Bamberger	Kirkwood	Emadi and Whiting	Spear and Gardner
	step 1	N	S	N	N
	step 2	S	S	S	N
	step 3	S	N	S	N
	step 4	S	S	N	N

Table D-33: Statistical Comparison Between Theoretical and Experimentally Determined SDAS For Zircon Sand Molds

Zircon Sand Mold	Model	Bamberger	Kirkwood	Emadi and Whiting	Spear and Gardner
	step 1	N	S	N	N
	step 2	S	S	N	S
	step 3	N	N	N	N
	step 4	S	N	N	N

Table D-34: Statistical Comparison Between Theoretical and Experimentally Determined SDAS For Copper Particulate Molds

Copper Particulate Mold	Model	Bamberger	Kirkwood	Emadi and Whiting	Spear and Gardner
	step 1	S	N	S	N
	step 2	S	N	S	N
	step 3	S	N	S	S
	step 4	S	S	S	N

The statistical analysis shows there is a significant difference between the SDAS calculated from Bamberger’s model and the SDAS determined experimentally for steps 2, 3, and 4 of the silica sand mold casting. Also, from Bamberger’s model, there is significant difference in steps 2 and 3 of the zircon sand mold castings and in every step of the copper particulate mold castings. There are only signs of an insignificant difference in step 1 of the silica sand mold castings and steps 1 and 3 of the zircon sand mold. Kirkwood’s model showed a significant difference between theoretical SDAS and experimental SDAS in step 1, 2, and 4 for silica sand mold castings, steps 1 and 2 of the zircon sand mold castings, and step 4 of the copper particulate mold castings. There was an insignificant difference in the theoretical SDAS and experimentally determined SDAS in step 1 of the silica sand mold castings, steps 1 and 3 of the zircon sand mold castings, and in steps 1, 2, and 3 of the copper particulate mold castings. Emadi and Whiting’s model showed a significant difference in steps 2 and 3 in the silica sand mold castings and every step of the copper particulate mold castings. However, Emadi and Whiting’s model did accurately predict the SDAS for every step in the zircon sand mold castings. Spear and Gardner’s model showed a significant difference only in step 2 of the zircon sand mold castings and in step 3 of the copper particulate castings. Spear and Gardner’s showed no significant differences between the theoretical SDAS and Experimental SDAS

for every step of the silica sand mold castings, steps 1, 3, and 4 of the zircon sand mold castings, and steps 1, 2, and 4 of the copper particulate mold castings.

From the statistical analysis, Bamberger’s model doesn’t appear to be an accurate model for predicting SDAS from the author’s work. Only three out of twelve steps showed no significant difference in the theoretical and experimental SDAS. While Kirkwood and Emadi and Whiting’s models faired slightly better than Bamberger’s, neither accurately predicted the SDAS from the castings made. Both models only showed six of the twelve steps to have no significant difference in the theoretical and experimentally determined SDAS. Spear and Gardner’s model showed only significant differences between the theoretical SDAS and experimental SDAS in two of the twelve steps cast. Spear and Gardner’s model appears to be the most accurate model for the author’s data. The corresponding F_0 values from each statistical test are given in Tables D-35, 36, and 37.

Table D-35: F_0 Values from comparison between SDAS from theoretical models and experimentally determined in a copper particulate mold

	F_0 Values			
Model	Bamberger	Kirkwood	Emadi and Whiting	Spear and Gardner
step 1	40.58	0.11	55.1	0.9
step 2	17.3	0.52	13.21	0
step 3	5305	4.42	3206	65.77
step 4	1526	14.5	735	2.67

Table D-36: F_0 Values from comparison between SDAS from theoretical models and experimentally determined in a silica sand mold

	F_0 Values			
Model	Bamberger	Kirkwood	Emadi and Whiting	Spear and Gardner
step 1	3.38	11.64	2.78	6.53
step 2	35.5	8.58	14.9	3.09
step 3	38.75	1.93	14.2	0.22
step 4	21.96	5.71	4.13	2.53

Table D-37: F_0 Values from comparison between SDAS from theoretical models and experimentally determined in a zircon sand mold

	F_0 Values			
Model	Bamberger	Kirkwood	Emadi and Whiting	Spear and Gardner
step 1	3.78	12.35	3.86	6.73
step 2	31.39	68.08	7.48	40.43
step 3	5.89	7.2	0.8	4.21
step 4	12.63	5.55	2.15	2.79

